PNAS
www.pnas.org

Supplementary Information for

Motor guidance by long-range communication on the microtubule highway

Sithara S. Wijeratne, Shane A. Fiorenza, Alex E. Neary, Radhika Subramanian, Meredith D. Betterton

Radhika Subramanian
E-mail: radhika@molbio.mgh.harvard.edu
Meredith D. Betterton
Email: mdb@colorado.edu

This PDF file includes:

Other supplementary materials for this manuscript include the following:

Supporting Information Text

Microtubule occupancy estimate. Using kymographs from experiments with only 20 pM Kif4A present, the single-molecule on-rate of Kif4A is estimated to be 3.6×10^{-4} $(\text{nM}{\cdot}\text{s})^{-1}$ per binding site. Binding sites correspond to a single tubulin dimer. Processive runs of Kif4A have an average duration of approximately 2 seconds, leading to an average off-rate of 0.5 per second. We can use these values to calculate the expected fractional occupancy $< n >$ of microtubule sites with the Scatchard equation:

$$< n >= \frac{k_{\text{on}} c}{k_{\text{off}} + k_{\text{on}} c}$$

where k_{on} is the per-site on-rate, k_{off} is the off-rate, and c is the bulk concentration of molecules in solution. Using the values listed above, the fractional occupancy of microtubules at a bulk motor concentration of 1 nM is expected to be less than 0.001. For an 8-μm-long microtubule, this would mean an average occupancy of just one binding site per protofilament. This is almost three orders of magnitude less than what is expected from the experimental line of best fit at the same motor concentration (Fig. 1C in main text). For a bulk motor concentration of 20 pM, the expected fractional occupancy is just 1.4×10^{-5}. This means we would need a microtubule over 500 μm long to see one bound motor per protofilament on average. It is difficult to see how short-range effects alone, regardless of the specific mechanism, could enhance microtubule occupancy to the experimentally-observed levels at picomolar concentrations without resulting in saturated microtubules at nanomolar concentrations.

Steady-state accumulation model. We can also consider an accumulation model of motors at steady state. To simplify the model and further demonstrate the need for some form of cooperativity, we assume that every motor that binds to the microtubule makes it to the plus-end and joins the end-tag, i.e., motors have infinite processivity until they reach the end-tag. We note that this processive run will take some time, but we consider it to be instantaneous when compared to the much longer timescale of motor binding events. We also assume that each motor occupies two binding sites, or 16 nm, within the end-tag. The steady-state rate of change of motors bound within the end-tag is then

$$0 = (N - 2n)k_{\text{on}}c - nk_{\text{off}}$$

where N is the total number of binding sites on the microtubule, n is the number of motors within the end-tag, k_{on} is the per-site on-rate of motors, c is the bulk motor concentration, and k_{off} is the motor off-rate within the end-tag. We use the same values of k_{on} and k_{off} as in the microtubule occupancy estimate above. We see that, even with numerous assumptions that favor end-tag formation, the off-rate within the end-tag needs to be reduced by a factor of 20 for end-tags to appreciably form (Fig. S2).

Computational Model

Microtubules. We model microtubules as single protofilaments, where each 8-nm tubulin dimer corresponds to a discrete binding site on a one-dimensional lattice. All binding sites have the same base binding affinity before binding interactions are taken into account. Microtubules are polar and have sites that correspond to a plus- and minus-end. The microtubule is assumed to be fixed in space and hydrodynamic interactions between motors are neglected (1, 2).

Motors. Each motor consists of two independently binding heads connected by a rigid linkage. Motors are implicitly modeled in solution and randomly drawn from an infinite reservoir upon binding. Motors bind to the microtubule with rate $k_{\text{on}}cn$, where k_{on} is the per-site on-rate of motors, n is the number of unoccupied binding sites available, and c is the bulk concentration of motors in solution. The first motor head to bind is always leading, i.e., closer to the plus-end than the unbound head. At any given time, motor heads can be bound to either ADP, ATP, ADP·Pi, or no ligand (empty). While in solution, both motor heads are assumed to be bound to ADP. Upon binding to the microtubule, the first motor head releases ADP and becomes empty. While empty or ATP-bound, motor heads are assumed to be strongly bound and cannot unbind from the microtubule. ATP binding to the empty head occurs at rate k_{ATP} and induces a conformational change that swings the second (unbound) head forward. The first (bound) head then hydrolyzes ATP to ADP·Pi at rate k_{hydro}. This is the rate-limiting step of the cycle, and thus k_{hydro} sets overall motor velocity. Next, the motor can either unbind its first (bound) head at rate $k_{\text{off},1}$, terminating its run, or bind its second (unbound) head to the microtubule at rate $k_{\text{on}}c_{\text{eff}}$, making it doubly bound and continuing its run. Here c_{eff} is the effective concentration of the unbound motor head when constrained to be near the microtubule by the bound head. The ratio between $k_{\text{off},1}$ and $k_{\text{on}}c_{\text{eff}}$ determines how many steps occur on average before the motor fully unbinds and thus overall motor processivity. While the motor is doubly bound, the rear head unbinds with rate $k_{\text{off},2}$ and the front head cannot unbind. Upon rear head unbinding, the motor is again in the singly bound state, after having advanced forward one site along the microtubule. Parameter values and descriptions are shown in Table S1. For a more detailed discussion, see Ref. 1.

Steric exclusion. No two motor heads can occupy the same binding site at the same time. We neglect any steric effects that do not directly occur on the microtubule lattice. For example, we assume the trailing head of a singly-bound motor can always swing forward during a conformational change, regardless of how crowded the surrounding solution is.

End-pausing. We model end-pausing by disabling the conformational change induced by ATP binding when a motor head is bound to the microtubule plus-end. The trailing head can still re-bind to the microtubule as long as the site remains unoccupied.

Short-range binding cooperativity. Short-range binding cooperativity in our model is a nearest-neighbor interaction with a range of one lattice site. The attractive potential has an energy of magnitude ϵ (written in units of $k_{\mathrm{B}}T$). We encode all energy-dependence into unbinding, giving

$$k_{\mathrm{on}} = k^0_{\mathrm{on}},$$
$$k_{\mathrm{off}} = k^0_{\mathrm{off}} \exp[-n\epsilon],$$

where $n = 0, 1, 2$ is the number of neighbors of the motor head. We assume that motor heads of the same motor do not interact cooperatively, so doubly-bound motor heads can have a maximum of one neighbor. The interaction only occurs between motors bound to the microtubule lattice. For a more detailed discussion, see Ref. 1.

Long-range binding cooperativity. To model long-range binding cooperativity, we use the potential

$$E(x) = \begin{cases} -E_0 \left[1 - \left(\frac{x}{D}\right)^2\right], & x \leq D \\ 0, & x > D \end{cases}$$

which is negative (attractive) up to the cutoff distance D and zero beyond it. Here x is the distance from the motor along the one-dimensional lattice and E_0 is the strength of the interaction energy in units of $k_{\mathrm{B}}T$. The effects of multiple motors superpose up a maximum E^*, which represents the upper limit at which long-range interactions saturate. We encode energy-dependence equally into binding and unbinding, giving

$$k_{\mathrm{on}} = k^0_{\mathrm{on}} \exp\left[\frac{1}{2} \min\{\textstyle\sum_i -E(x_i),\, E^*\}\right],$$
$$k_{\mathrm{off}} = k^0_{\mathrm{off}} \exp\left[-\frac{1}{2} \min\{\textstyle\sum_i -E(x_i),\, E^*\}\right],$$

where x_i is the distance from the i^{th} nearby motor. Unless otherwise stated, this long-range interaction is always implemented alongside the short-range binding cooperativity described above. For a more detailed discussion, see Ref. 1.

Long-range stepping cooperativity. Motor interactions that affect stepping could occur via multiple plausible mechanisms, but the resulting conclusions would be similar as long as the interaction works to lower motor stepping speed. We modeled one plausible hypothesis for the mechanism: the internal necklinker tension that couples motor heads could somehow be decreased by the interaction. To implement this, we extended the model of necklinker tension in motor stepping by Andreasson et al. (3). Our changes modify the rear-head unbinding rate of doubly bound motors to

$$k_{\mathrm{off},2} = k^0_{\mathrm{off},2} \exp[F_{\mathrm{int}} \delta_{\mathrm{off}} / k_{\mathrm{B}}T],$$

and introduce a new doubly bound → partially docked pathway with rate

$$k_{\mathrm{ATP},2} = k^0_{\mathrm{ATP}} \exp[-F_{\mathrm{int}} \delta_{\mathrm{ATP}} / k_{\mathrm{B}}T],$$

where F_{int} is the internal necklinker tension, and δ_{off} and δ_{ATP} are unbinding and ATP-binding distance parameters, respectively. When ATP binds to the front head, the rear head detaches from the microtubule and swings forward, skipping the singly bound state. The rate of this transition is normally close to zero. However, if we allow the long-range interaction to reduce internal necklinker tension, the doubly bound ATP-binding rate increases to a non-negligible value. We implement the change in necklinker tension by multiplying the doubly bound ATP-binding rate and off-rate by $\exp\left[\frac{1}{2} \min\{\sum_i -E(x_i),\, E^*\}\right]$ and $\exp\left[-\frac{1}{2} \min\{\sum_i -E(x_i),\, E^*\}\right]$, respectively. For a more detailed discussion, see Ref. 1.

Approach to steady state. Simulations run for a time t_{e} to pre-equilibrate (approach steady state in binding). The fractional occupancy of the microtubule, defined as the number of occupied binding sites divided by the total number of binding sites, is averaged over this time. At the end of pre-equilibration, fractional occupancy is calculated and stored each timestep. Every t_{c} seconds after, the average and standard deviation of fractional occupancy are calculated. If the change in average fractional occupancy is less than the standard deviations added in quadrature, the system is considered equilibrated. At this point, data collection begins and continues until the end of the simulation.

Simulated end-tag analysis. End-tags were first allowed to reach a steady-state and data were then recorded until 500 processive kinesin runs had been recorded in the simulation. Microtubule occupancy data are averaged over all points to determine steady-state fractional occupancy. These occupancy data are smoothed with a moving average window 250-nm wide, chosen to match the diffraction limit of visible light. Starting from the plus-end of the microtubule, the first site past peak occupancy with a slope less than half the peak slope is considered the end-tag boundary (Movie S3).

Simulated fluorescence images. The motor fractional occupancy is averaged for 0.5 seconds to mimic image collection time. We then apply a Gaussian filter to the average motor occupancy to create the cyan channel of the image. We repeat this process for a fully occupied array to create the magenta channel, meant to represent tubulin. The yellow channel is made up of random noise. The simulated fluorescence image is a merge of these three channels, and movies are generated by arranging images in sequence

Supplementary Methods

Protein purification. Recombinant proteins (Kif4A, Kif4A-GFP, Kif4A-mCherry, Kif4A-CLIP, K401, K401-CLIP) were expressed and purified as described previously (4, 5). For CLIP protein labeling, purified protein was incubated with CLIP-Surface™ 647 in a 1:3 (protein:dye) molar ratio, at 30°C for 1 hr, followed by incubation at 4°C overnight. Unbound dye was removed by repeated dilution and centrifugation through an Amicon Ultra-15 Centrifugal Filter Unit (Millipore Sigma), prior to size exclusion chromatography. A comparison of the absorbance of pure labeled protein at 650 nm and 280 nm yielded a labeling efficiency of 15% and 58% per monomer for two independent protein preparations. Since K401 is a dimer, this corresponds to 15-28% and 58-82% labeling of the dimeric motors in our preparation.

Microtubule polymerization. Taxol-stabilized rhodamine-labeled microtubules were prepared with biotin tubulin as described previously (5). Briefly, GMPCPP seeds were prepared from a mixture of unlabeled bovine tubulin, X-rhodamine-tubulin and biotin tubulin, which were diluted in BRB80 buffer (80 mM PIPES pH 6.8, 1.5 mM $MgCl_2$, 0.5 mM EGTA, pH 6.8) and mixed together by tapping gently. The tube was transferred to a 37°C heating block and covered with foil to reduce light exposure. The biotinylated microtubules were incubated for 1 hr. Afterwards, 100 μL of warm BRB80 buffer was added to the microtubules and spun at 75000 rpm, 10 min, and 37°C to remove free unpolymerized tubulin. Following the centrifugation step, the supernatant was discarded, and the pellet was washed by a round of centrifugation with 100 μL BRB80 supplemented with 20 μM taxol. The pellet was resuspended in 16 μL of BRB80 containing 20 μM taxol and stored at room temperature covered in foil.

In vitro fluorescence microscopy assay. The microscope slides (Gold Seal Cover Glass, 24 × 60 mm, thickness No. 1.5) and coverslips (Gold Seal Cover Glass, 18 × 18 mm, thickness No. 1.5) were cleaned and functionalized with biotinylated PEG and non-biotinylated PEG, respectively, to prevent nonspecific surface sticking, according to standard protocols. Flow chambers were built by applying two strips of double-sided tape to a slide and applying to the coverslip. Sample chamber volumes were approximately 6–8 μL. To observe the end-tag accumulation of Kif4A on microtubules, rhodamine-labeled biotinylated microtubules were immobilized in a flow chamber coated with neutravidin (0.2 mg/ml). Next, Kif4A-GFP and and 1 mM ATP were flushed into the flow chamber in assay buffer (BRB80 buffer supplemented with 1 mM TCEP, 0.2 mg/ml k-casein, 20 μM taxol, 40 mg/ml glucose oxidase, 35 mg/ml glucose catalase, 0.5% β-mercaptoethanol, 5% sucrose, and 1 mM ATP). The flow cell was incubated for 10 min before taking snapshots of the microtubule and GFP channel. To visualize single molecules, Kif4A-GFP and 1 mM ATP were flowed into the chamber and a time-lapse sequence of images was immediately acquired at a rate of 0.3 frames/s. Experiments with Kif4A-mCherry and K401-clip-647 were also performed using the same method. All experiments were performed on a Nikon Ti-E inverted microscope with a Ti-ND6-PFS perfect focus system equipped with an APO TIRF 100x oil/1.49 NA objective (Nikon). The microscope was outfitted with a Nikon-encoded x-y motorized stage and a piezo z-stage. High motor density experiments were performed using an sCMOS camera (Andor Zyla 4.2). Single molecule experiments were performed using an ANDOR iXon Ultra EMCCD camera (Lasers: 488 nm, 561 nm, and 640 nm; Filters: Single Band: 488 TIRF exciter, 561 TIRF exciter, and Quad Band: 405/488/561/640 TIRF exciter).

Kymograph image analysis. Fiji (NIH) was used to process the image files. Briefly, raw time-lapse images were converted to TIFF files. A rolling ball radius background subtraction of 50 pixels was applied to distinguish the features in the images more clearly. From these images, individual microtubules were picked and kymographs generated by the MultipleOverlay and MultipleKymograph plug-ins (J. Reitdorf and A. Seitz). We then extracted parameters such as run length and lifetime, and calculated the average velocity (run length/lifetime), for the observed single molecule tracks. The single molecule intensity distributions (Fig. S18) were determined by measuring the average integrated intensity of the first three pixels from single molecule GFP tracks in kymographs (Figs. 2A and 3A). We only included moving single molecule events, and excluded stalled events and events that accumulate at the microtubule ends from the analysis.

Single particle tracking analysis. The single molecule analysis was repeated with TrackMate, a Fiji plugin, to directly extract lifetime and velocity of events from the time-lapse images and confirm the results of the kymograph-based analysis (http://fiji.sc/TrackMate). Briefly, the microtubule channel was used to mark a region around a specific microtubule for single particle tracking. For the selection, we excluded the microtubule plus-end, which is indicated by the end with protein accumulation. Using the marked regions from the microtubule channel, the protein channel was used to track single particles by TrackMate on microtubules. To detect spots, the differences of the Gaussian (DoG) algorithm was used. For this detection method, spot sizes of 0.8 μm in diameter and sub-pixel localization were set. After the initial segmentation, the Quality filter, a measure of spot relevance, was used to further eliminate spurious spots. To form links from selected spots, the simple linear assignment problem (LAP) algorithm with a gap-closing max frame gap of 2, was used. For single particle events on a microtubule, spots, links and tracks output files were generated. The spots file contains intensities of spots of each track. The links contain instantaneous velocities of links between spots for each track. The tracks contain run lengths, lifetimes and average velocities of each track.

The data files were then further analyzed using MATLAB. The program first reads the input tracks, links and spot files. Next, the tracks are filtered by spot intensities to exclude tracks with aggregate events. Afterwards, to exclude pause events, the tracks with zero displacements were discarded. Also, to remove short events, tracks containing fewer than 3 frames were excluded. From the filtered tracks, the instantaneous velocities of each track were used to separate tracks according to three different event types. For “move events”, tracks with instantaneous velocities which were greater than 5 nm/s were included.

For "move with pauses events", instantaneous velocities less than 5 nm/s were included. For "all events", both move events and move events with pauses were included. After the separation of each event type, histograms of the run lengths, lifetimes, average velocities and associated instantaneous velocities and intensities of tracks were plotted. Run lengths and lifetimes histograms were fit to exponential fits, and the velocity histograms were fit to Gaussian distributions.

Co-localization analysis. For experiments in which motors with two different fluorophores were imaged near simultaneously, we quantified the percent of co-localization of fluorescence signals between two channels (Fig. 4G and H). Briefly, microtubules were identified using the fluorescence signal from tubulin. The region of the microtubule excluding the end-tag was selected for further analysis. Kymographs from GFP and either Alexa-647 or mCherry channel were analyzed for colocalization at each time frame. The GFP kymograph was selected as channel 1 and the mCherry or clip-647 kymograph was selected as channel 2. Each of the channels were converted to a binary image, so that the tracks are clearly visible. To visually distinguish the overlap region of clip-647/mCherry fluorescence signal on GFP tracks (channel 2 on channel 1), the pixels in the GFP channel were colored green, and the pixels in the mCherry/clip-647 channels were converted to red. When both the green and red channels are combined into a composite kymograph, the yellow pixels in the combined image indicate the location of the overlapped pixels. Using this image, the quantification of the co-localization of the clip-647/mCherry fluorescence signal on GFP tracks (channel 2 on channel 1) was analyzed in two different ways. In the first method, the percentage of pixels for which a fluorescence signal corresponding to K401/Kif4A-mCherry seen along a Kif4A-GFP track was calculated [number of yellow pixels divided by the number of green pixels]. In the second method, the co-movement of motors only if the overlap is at least 5 consecutive pixels was calculated [number of yellow pixels (tracks longer than 5 pixels) divided by the number of continuous green pixels (tracks longer than 5 pixels)]. The percentage colocalization values were compiled into a bar graph, and the mean and the standard error of the mean were calculated.

BioLayer Interferometry (BLI) Assays. The BLI assays were performed in an Octet Red 96 instrument (ForteBio). The ligand proteins, K401 or full-length PRC1-2 (positive control) were immobilized on an amine-reactive, second-generation sensor (AR2G Reagent kit; ForteBio) at 12 μg/ml in sodium acetate buffer (pH 5.0). The analyte protein (Kif4A-GFP) was diluted in the binding buffer: 1× BRB80 (80 mM K-PIPES pH 7.2, 1 mM $MgCl_2$, and 1 mM EGTA) with 50 mM KCl, 1 mM DTT, 1 mM ATP, and 0.1% Tween, at 500 nM. First, the ligand-bound sensors were dunked in 1 M ethanolamine quenching solution and then a pre-blocking binding buffer with 1 mg/ml α-casein, to reduce nonspecific binding of analyte. Following these steps, the sensor was next dipped in the binding buffer and afterwards into analyte (Kif4A-GFP) to record the binding response for the association of analyte to ligand, and then into plain binding buffer for dissociation. To measure the nonspecific binding of the analyte (Kif4A), the assay was repeated without ligand (K401 or PRC1). Data Analysis 9.0 software (ForteBio) was used for data analysis, and double referencing was performed to correct for drift of ligand from sensor and nonspecific binding of analyte. Binding responses from association step and dissociation step were plotted over time.

Photobleaching experiments. The fluorescent protein was non-specifically adhered to a glass coverslip at low density such that single molecules could be resolved. After washing away unbound protein, imaging buffer (BRB80 supplemented with 1 mM DTT, 40 mg/ml glucose oxidase, 35 mg/ml glucose catalase, 0.5% β-mercaptoethanol, 5% sucrose, and 1 mM ATP) was added to the chamber and images were acquired at 0.20 s intervals on an ANDOR iXon Ultra EMCCD camera with EM gain set to 287. To detect the fluorescence spots, the first image of the stack was background subtracted and a Fiji plugin, MOSAICsuite particle tracking module (https://imagej.net/plugins/mosaicsuite) was used to generate the spot centers. The detected spot centers were imported to MATLAB where code was implemented to calculate the average integrated intensity and generate the intensity versus time profiles of each spot. Briefly, the program first reads the image stack and loads the spot center data. It then discards all the spots at the edge of the image stack, and performs a local background subtraction of each spot. From the background subtracted data, the average integrated intensity is calculated from the first three frames of the image stack. The final intensity values were compiled into a histogram and the mean values and error were calculated using a log normal fit to the distribution.

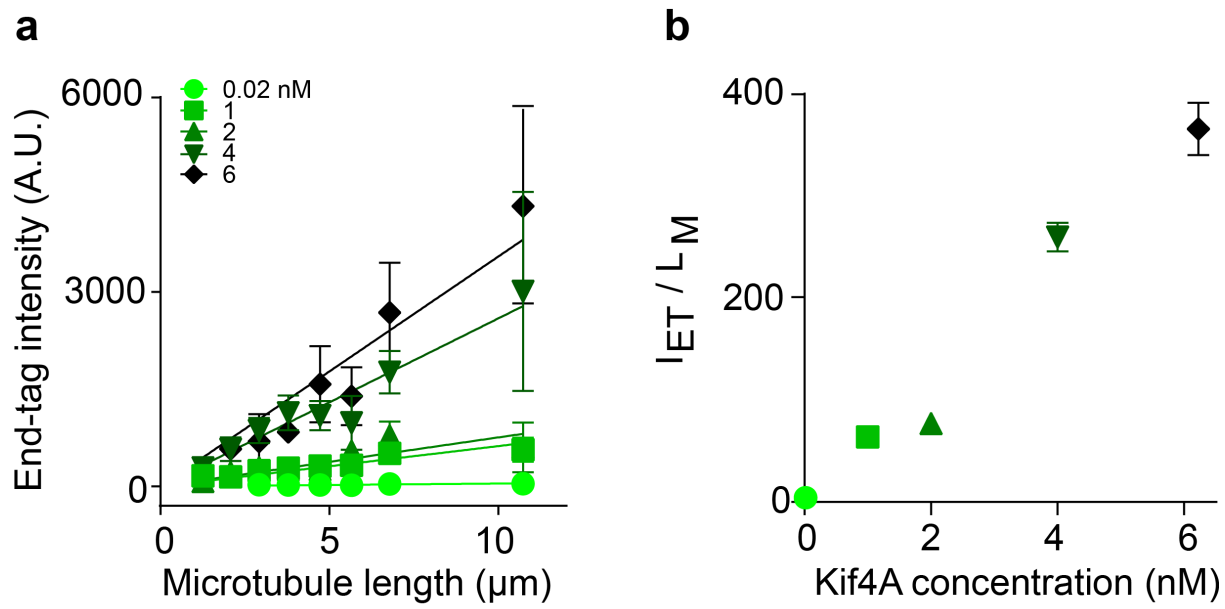

Fig. S1. (A) End-tag intensity versus microtubule length from assays with Kif4A-GFP concentration from 0.02 to 6 nM: 0.02 nM (circles: slope 4.44 ± 0.50; N=29), 1 nM (squares: slope 62.2 ± 4.39; N=46), 2 nM (triangles: slope 75.6 ± 9.39; N=30), 4 nM (inverted triangles: slope 259 ± 14.2; N=78), and 6 nM (diamonds: slope 355 ± 26.0; N=64). (B) Slope of plots of end-tag intensity versus microtubule length from (A) as a function of Kif4A concentration. The data points in (A) represent the binned averages of the end-tag lengths of many microtubules. The error bars represent the standard deviation of the experimental data.

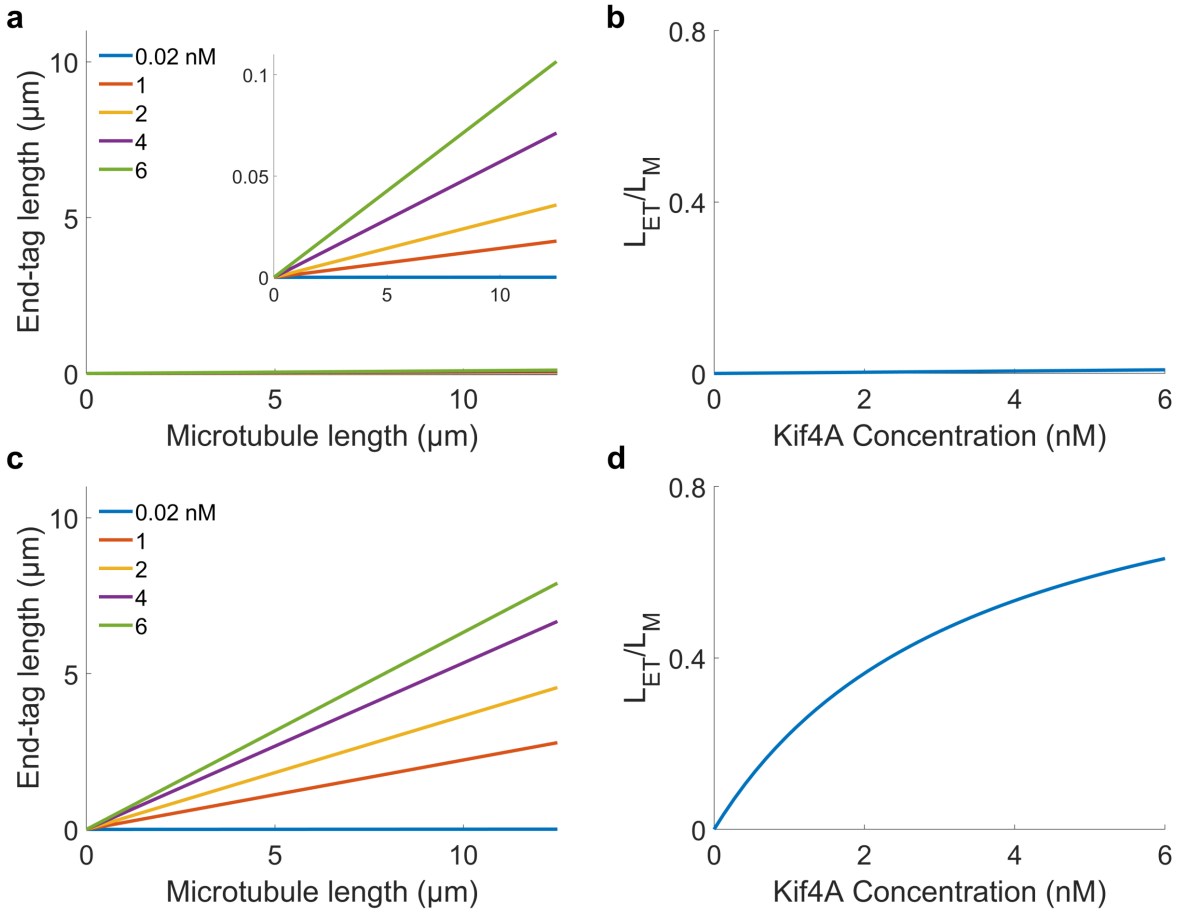

Fig. S2. (A) End-tag length predicted by simplified steady-state accumulation model (see supplementary text) versus microtubule length using "wild-type" parameters and experimental Kif4A bulk concentration. Inset: end-tag length versus microtubule length with adjusted y-axis to better show the difference between concentrations. (B) Slope of end-tag length predicted by simplified steady-state accumulation model versus bulk Kif4A motor concentration using wild-type parameters. (C) End-tag length predicted by simplified steady-state accumulation model versus microtubule length with motor off-rate within the end-tag reduced by a factor of 20. (D) Slope of end-tag length predicted by simplified steady-state accumulation model versus bulk Kif4A motor concentration with motor off-rate within the end-tag reduced by a factor of 20.

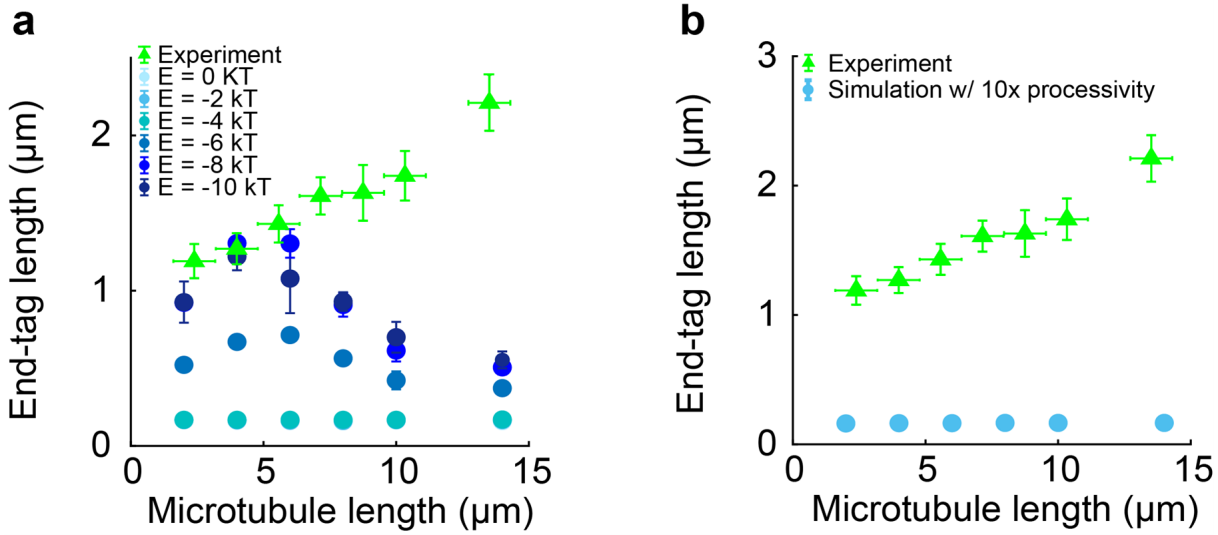

Fig. S3. (A) End-tag length versus microtubule length from simulations with nearest-neighbor interactions of varying strength (blue circles) and experiment (green triangles). (B) End-tag length versus microtubule length from simulations with motor processivity increased by a factor of 10 (blue circles) and experiment (green triangles). Simulation data points represent the average of four independent runs. Error bars represent the standard error of the mean.

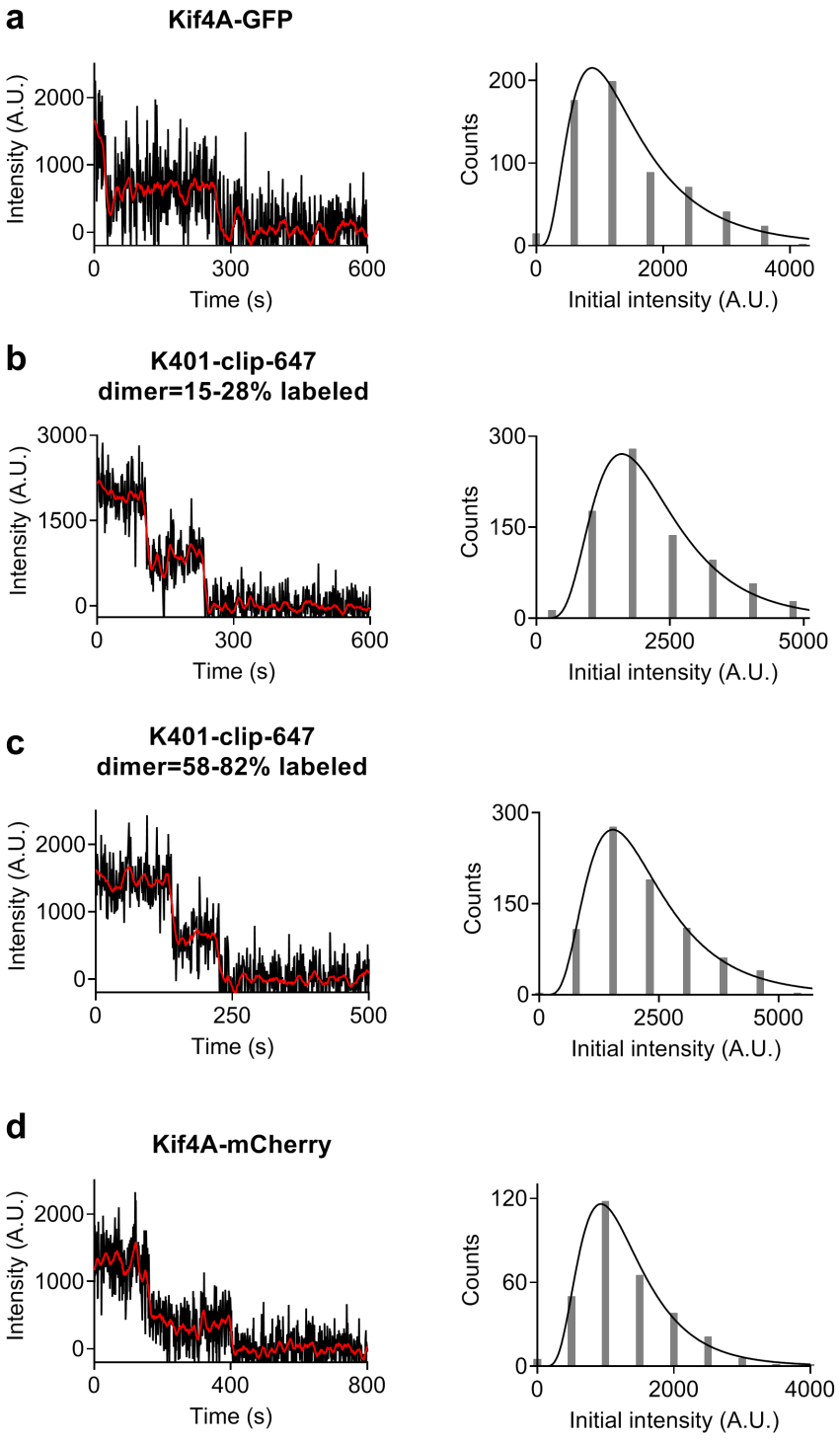

Fig. S4. Single molecule photobleaching traces and single molecule initial intensity distributions for (A) Kif4A-GFP (Mean: 1400 ± 70 A.U., N=670), (B) K401-clip-647-15-28% labeled dimer (2000 ± 80 A.U., N=787), (C) K401-clip-647-58-82% labeled dimer (2000 ± 40 A.U., N=786), and (D) Kif4A-mCherry (Mean: 1200 ± 30 A.U., N=303). Background-subtracted fluorescence intensity versus time plots were used for step photobleaching analysis. The mean and error were determined by the log-normal fit to the histograms.

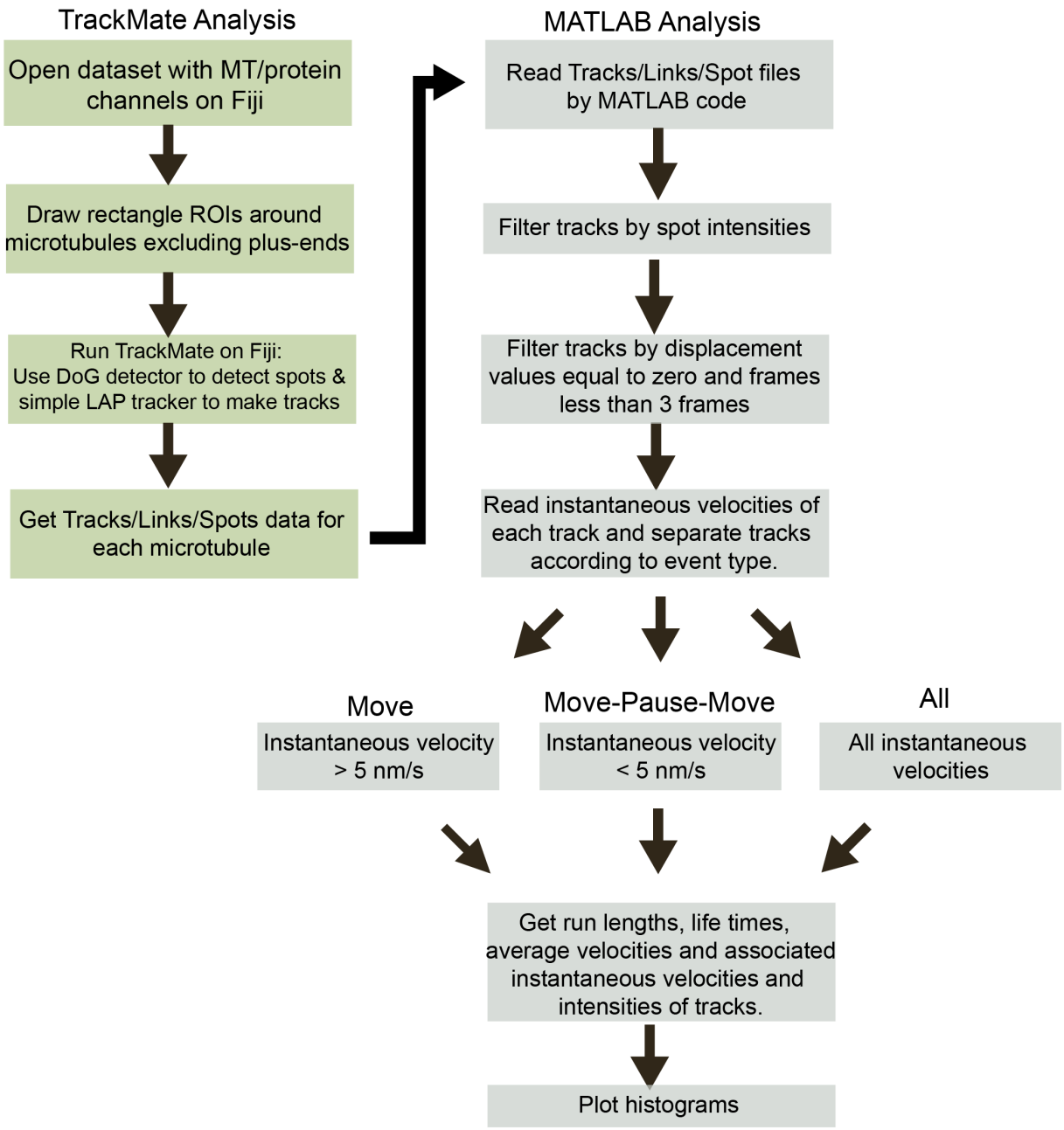

Fig. S5. Data processing pipeline for single particle tracking and analysis of run lengths, lifetimes and velocities. The single molecule analysis was repeated with TrackMate, a Fiji plugin, to directly extract lifetime and velocity of motors from the time-lapse images and confirm the results of the kymograph analysis (http://fiji.sc/TrackMate). MATLAB was used to further analyze the events and separate tracks according to three different event types (see supplementary methods).

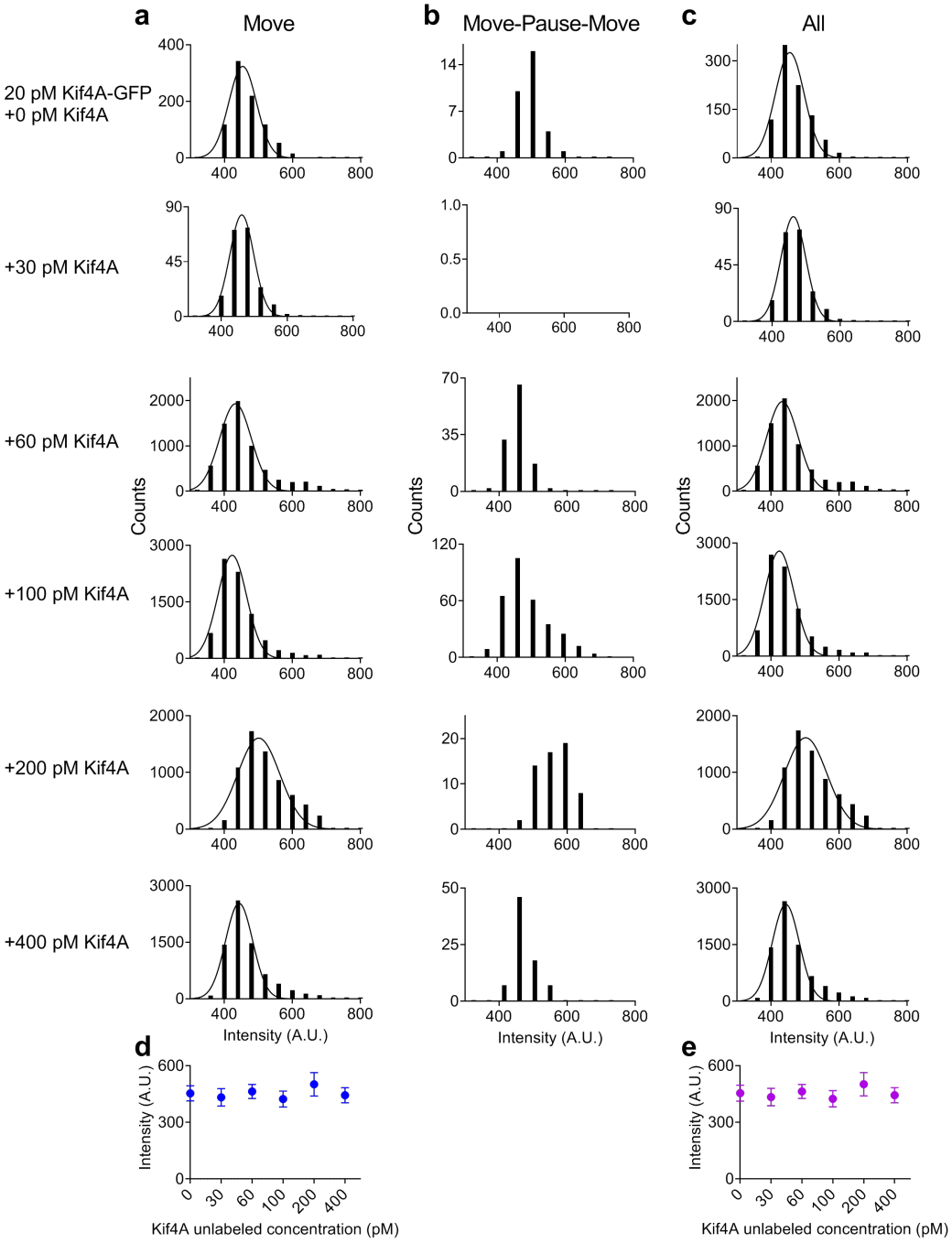

Fig. S6. Histograms of the motor spot intensity for (A) Move, (B) Move-Pause-Move and (C) All events obtained from time-lapse image sequence acquired in examining microtubule interaction of Kif4A-GFP (20 pM) in presence of 0, 30, 60, 100, 200 and 400 pM Kif4A-unlabeled molecules by single particle tracking. The average intensity histograms were fit to Gaussian distributions. (D) Intensity versus Kif4A concentration, obtained from Gaussian fits in (A): 0 pM (453 ± 41 A.U., N=875), 30 pM (463 ± 37 A.U., N=199), 60 pM (433 ± 47 A.U., N=6473), 100 pM (423 ± 43 A.U., N=7857), 200 pM (501 ± 62 A.U., N=6495) and 400 pM (443 ± 40 A.U., N=7097). (E) Intensity versus Kif4A concentration, obtained from Gaussian fits in (C): 0 pM (455 ± 42 A.U., N=907), 30 pM (463 ± 37 A.U., N=199), 60 pM (433 ± 46 A.U., N=6592), 100 pM (424 ± 43 A.U., N=8173), 200 pM (502 ± 63 A.U., N=6555) and 400 pM (444 ± 40 A.U., N=7175). The error bars represent the standard deviation.

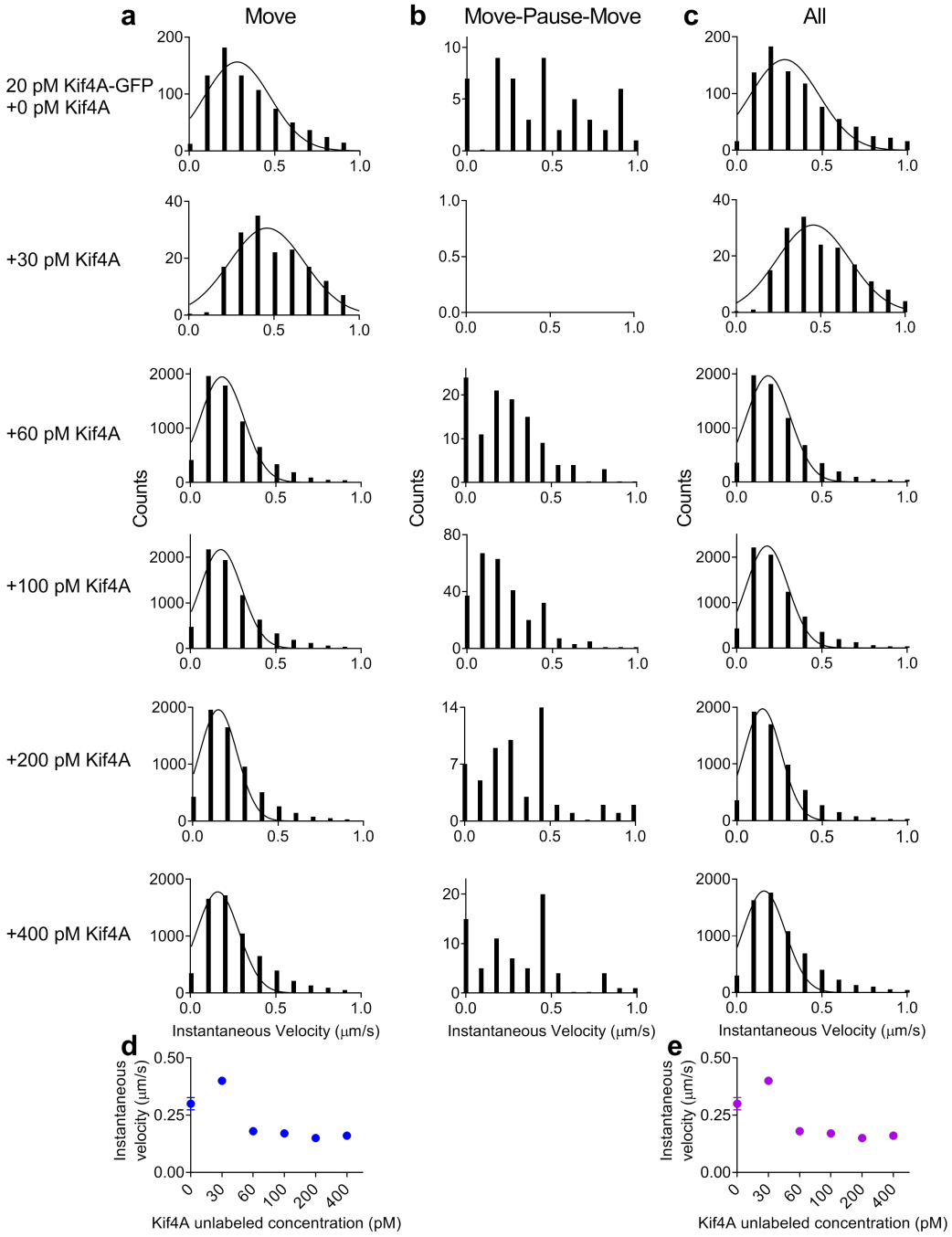

Fig. S7. Histograms of the instantaneous velocity for (A) Move, (B) Move-Pause-Move and (C) All events obtained from time-lapse image sequence acquired in examining microtubule interaction of Kif4A-GFP (20 pM) in presence of 0, 30, 60, 100, 200 and 400 pM Kif4A-unlabeled molecules by single particle tracking. The instantaneous velocity histograms were fit to Gaussian distributions. (D) Instantaneous velocity versus Kif4A concentration, obtained from Gaussian fits in (A): 0 pM (0.30 ± 0.03 μm/s, N=875), 30 pM (0.40 ± 0.02 μm/s, N=167), 60 pM (0.18 ± 0.01 μm/s, N=7197), 100 pM (0.17 ± 0.01 μm/s, N=7857), 200 pM (0.15 ± 0.01 μm/s, N=6495) and 400 pM (0.16 ± 0.02 μm/s, N=7097). (E) Instantaneous velocity versus Kif4A concentration, obtained from Gaussian fits in (C): 0 pM (0.30 ± 0.03 μm/s, N=956), 30 pM (0.40 ± 0.02 μm/s, N=167), 60 pM (0.19 ± 0.0.01 μm/s, N=7316), 100 pM (0.17 ± 0.01 μm/s, N=8173), 200 pM (0.15 ± 0.01 μm/s, N=6555) and 400 pM (0.16 ± 0.02 μm/s, N=7175). The error bars represent the standard error of the mean.

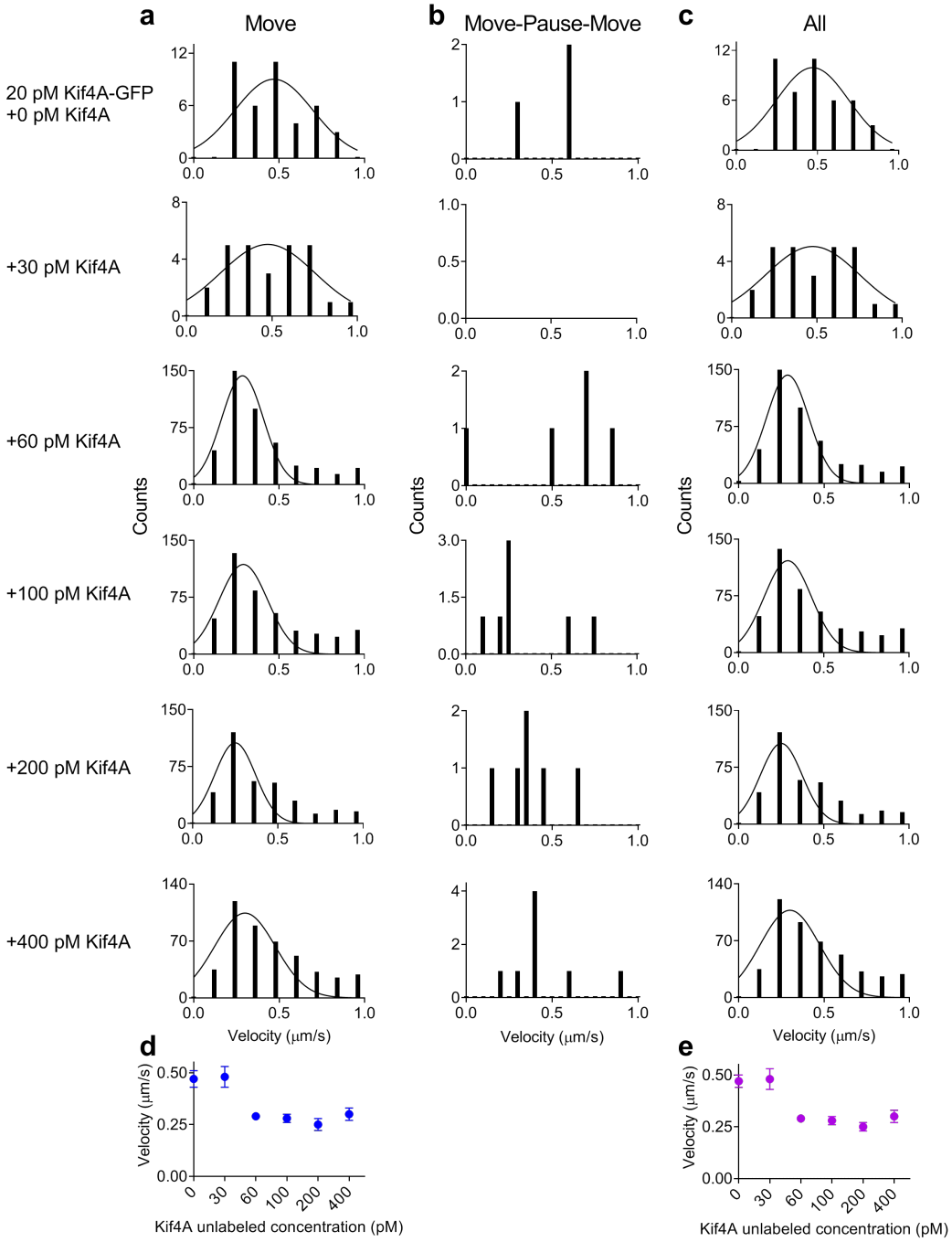

Fig. S8. Histograms of the velocity for (A) Move, (B) Move-Pause-Move and (C) All events obtained from time-lapse image sequence acquired in examining microtubule interaction of Kif4A-GFP (20 pM) in presence of 0, 30, 60, 100, 200 and 400 pM Kif4A-unlabeled molecules by single particle tracking. The velocity histograms were fit to Gaussian distributions. (D) Velocity versus Kif4A concentration, obtained from Gaussian fits in (A): 0 pM (0.47 ± 0.03 μm/s, N=53), 30 pM (0.48 ± 0.05 μm/s, N=27), 60 pM (0.28 ± 0.02 μm/s, N=510), 100 pM (0.28 ± 0.02 μm/s, N=520), 200 pM (0.25 ± 0.03 μm/s, N=397) and 400 pM (0.30 ± 0.03 μm/s, N=546). (E) Velocity versus Kif4A concentration, obtained from Gaussian fits in (C): 0 pM (0.47 ± 0.03 μm/s, N=57), 30 pM (0.48 ± 0.03 μm/s, N=27), 60 pM (0.29 ± 0.02 μm/s, N=516), 100 pM (0.28 ± 0.02 μm/s, N=531), 200 pM (0.25 ± 0.03 μm/s, N=403) and 400 pM (0.30 ± 0.03 μm/s, N=554). The error bars represent the standard error of the mean.

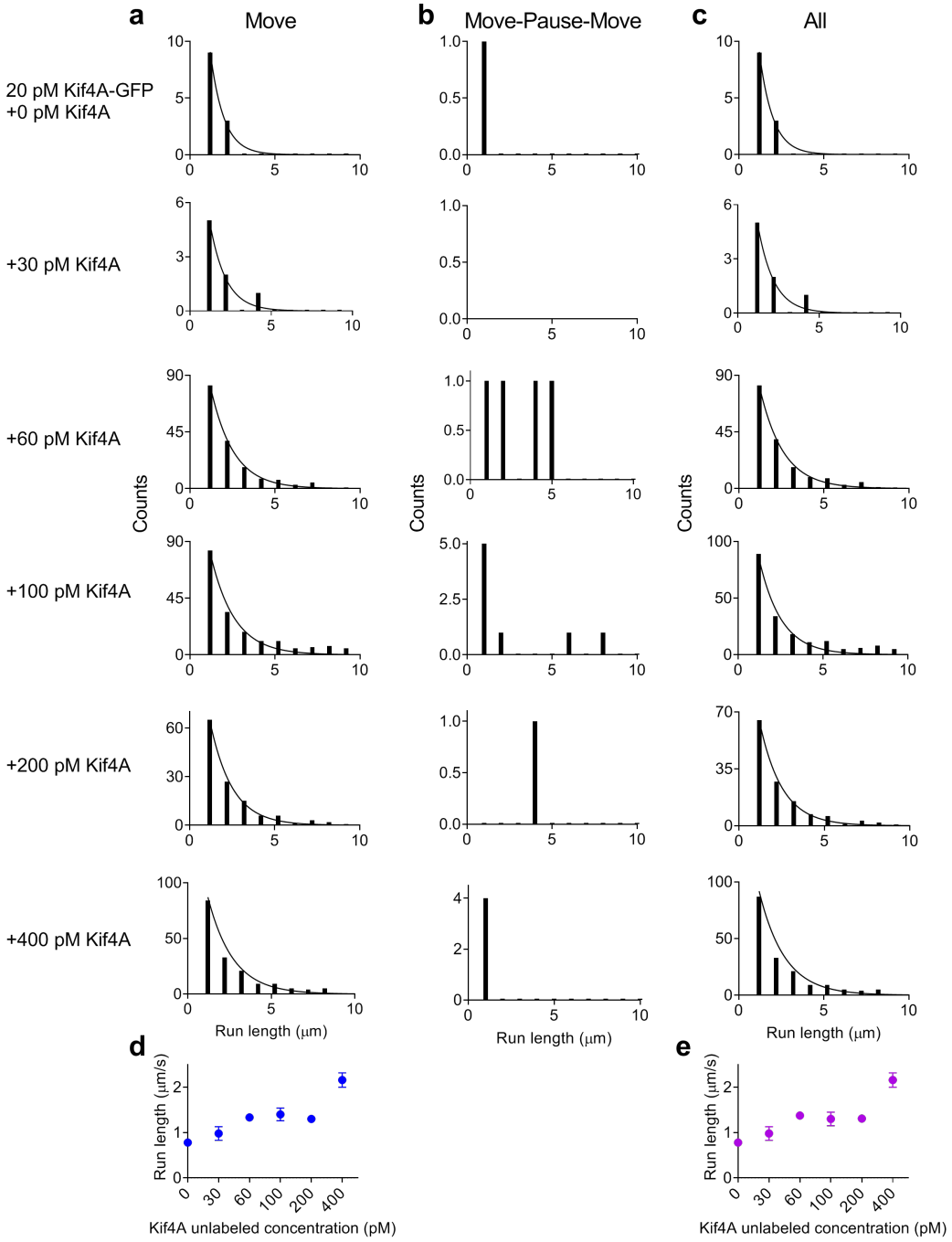

Fig. S9. Histograms of the run length for (A) Move, (B) Move-Pause-Move (C) and All events obtained from time-lapse image sequence acquired in examining microtubule interaction of Kif4A-GFP (20 pM) in presence of 0, 30, 60, 100, 200 and 400 pM Kif4A-unlabeled molecules by single particle tracking. The run length histograms were fit to exponential fits. (D) Run length versus Kif4A concentration, obtained from exponential fits in (A): 0 pM (0.78 ± 0.06 nm, N=49), 30 pM (0.98 ± 0.15 nm, N=27), 60 pM (1.3 ± 0.06 nm, N=510), 100 pM (1.4 ± 0.15 nm, N=520), 200 pM (1.3 ± 0.07 nm, N=397) and 400 pM (1.5 ± 0.16 nm, N=371). (E) Run length versus Kif4A concentration, obtained from exponential fits in (C): 0 pM (0.78 ± 0.06 nm, N=53), 30 pM (0.98 ± 0.15 nm, N=27), 60 pM (1.4 ± 0.07 nm, N=516), 100 pM (1.3 ± 0.16 nm, N=531), 200 pM (1.3 ± 0.07 nm, N=403) and 400 pM (1.5 ± 0.17 nm, N=379). The error bars represent the standard error of the mean.

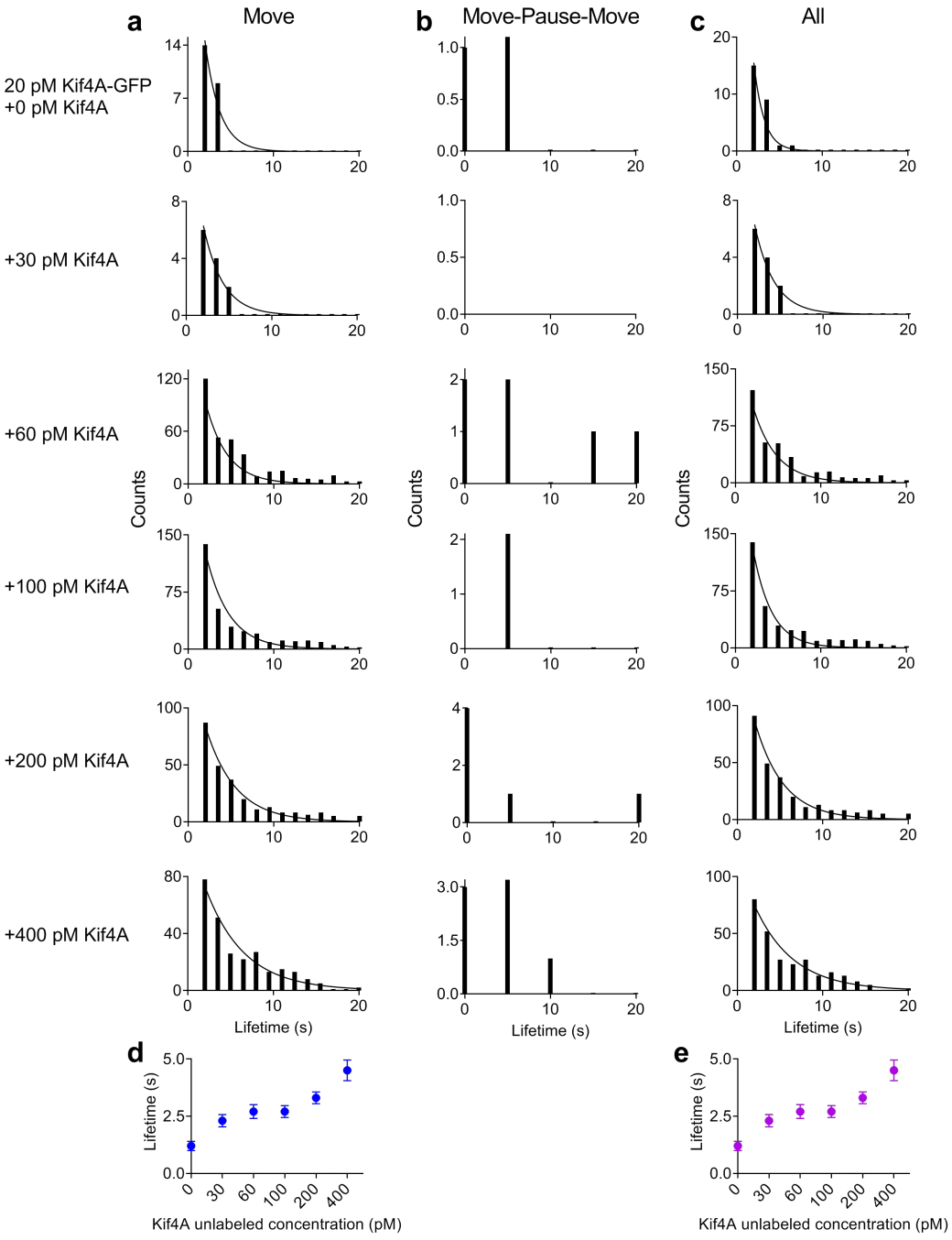

Fig. S10. Histograms of the lifetime for (A) Move, (B) Move-Pause-Move and (C) All events obtained from time-lapse image sequence acquired in examining microtubule interaction of Kif4A-GFP (20 pM) in presence of 0, 30, 60, 100, 200 and 400 pM Kif4A-unlabeled molecules by single particle tracking. The lifetime histograms were fit to exponential fits. (D) Lifetime versus Kif4A concentration, obtained from exponential fits in (A): 0 pM (1.7 ± 0.30 s, N=44), 30 pM (2.3 ± 0.27 s, N=27), 60 pM (2.5 ± 0.60 s, N=510), 100 pM (2.7 ± 0.35 s, N=520), 200 pM (3.5 ± 0.26 s, N=397) and 400 pM (4.5 ± 0.47 s, N=371). (E) Lifetime versus Kif4A concentration, obtained from exponential fits in (C): 0 pM (1.2 ± 0.30 s, N=48), 30 pM (2.3 ± 0.27 s, N=27), 60 pM (2.7 ± 0.50 s, N=516), 100 pM (2.1 ± 0.26 s, N=531), 200 pM (3.3 ± 0.26 s, N=403) and 400 pM (4.5 ± 0.46 s, N=379).

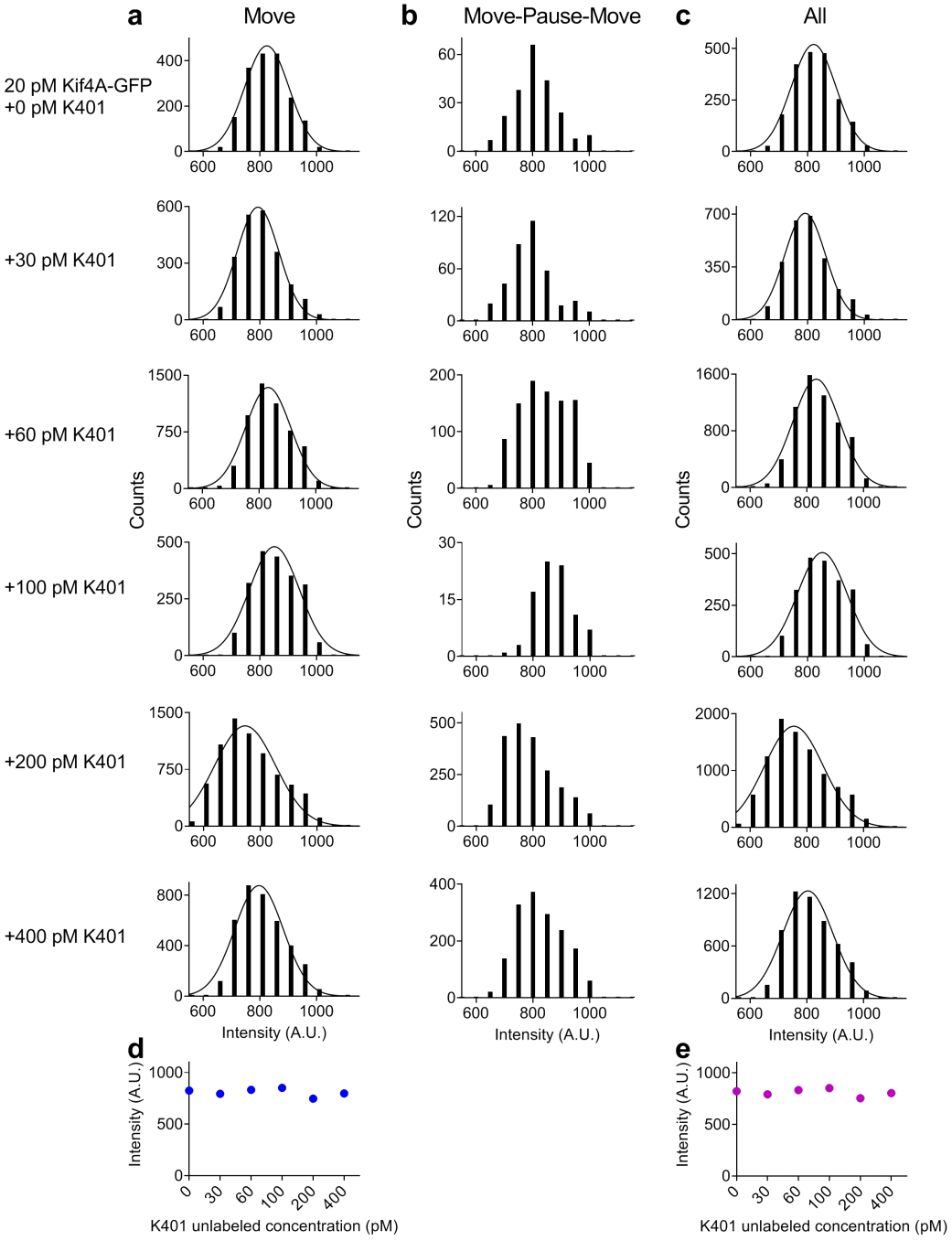

Fig. S11. Histograms of the intensity for (A) Move, (B) Move-Pause-Move and (C) All events obtained from time-lapse image sequence acquired in examining microtubule interaction of Kif4A-GFP (20 pM) in presence of 0, 30, 60, 100, 200 and 400 pM K401-unlabeled molecules by single particle tracking. The average intensity histograms were fit to Gaussian distributions. (D) Intensity versus K401 concentration, obtained from Gaussian fits in (A): 0 pM (824 ± 78 A.U., N=1803), 30 pM (793 ± 74 A.U., N=2230), 60 pM (832 ± 80 A.U., N=5265), 100 pM (851 ± 88 A.U., N=2045), 200 pM (747 ± 107 A.U., N=7091) and 400 pM (797 ± 86 A.U., N=3719). (E) Intensity versus K401 concentration, obtained from Gaussian fits in (C): 0 pM (822 ± 79 A.U., N=2022), 30 pM (792 ± 72 A.U., N=2606), 60 pM (833 ± 83 A.U., N=6225), 100 pM (852 ± 88 A.U., N=2133), 200 pM (754 ± 104 A.U., N=9226) and 400 pM (804 ± 88 A.U., N=5351). The error bars represent the standard deviation.

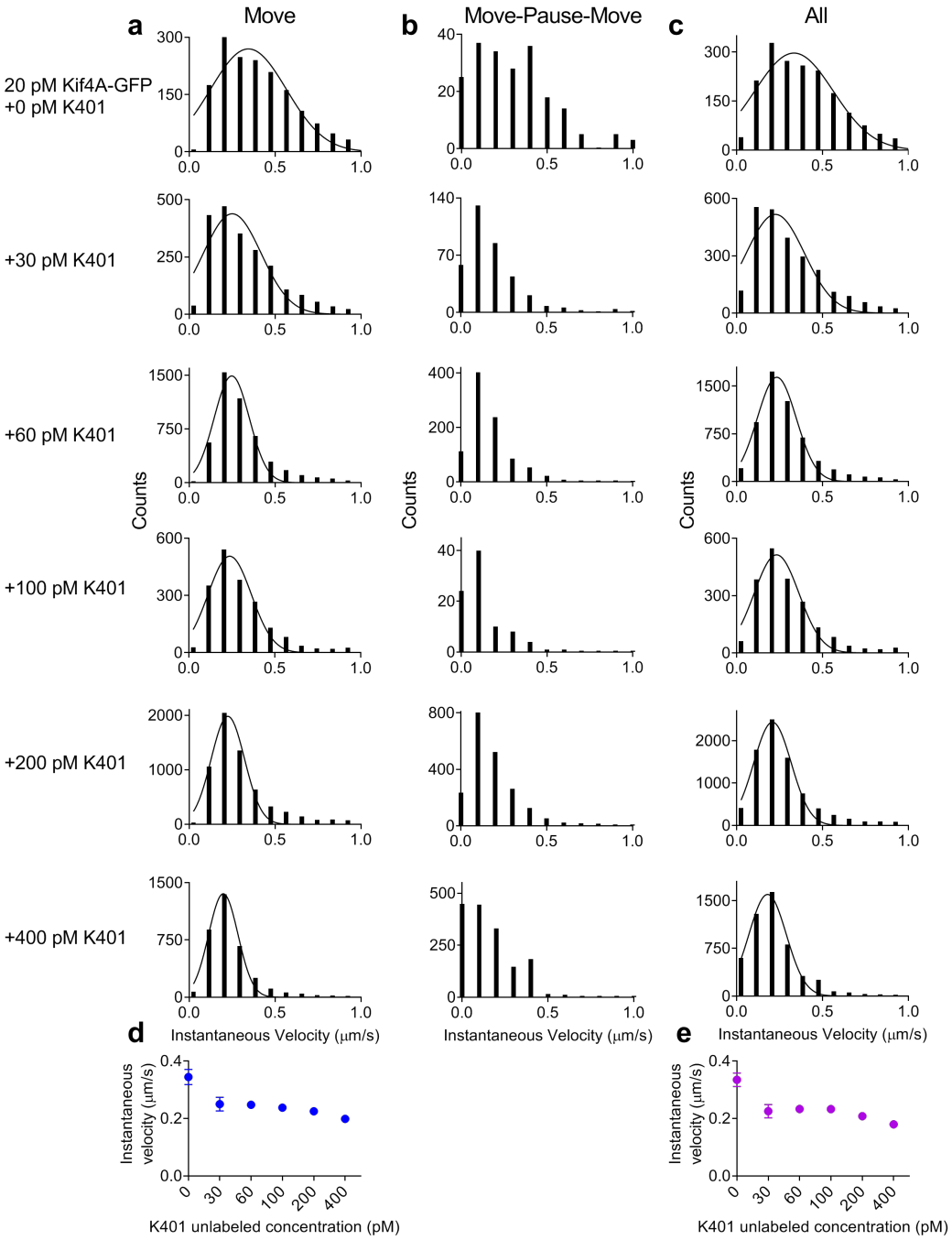

Fig. S12. Histograms of the instantaneous velocity for (A) Move, (B) Move-Pause-Move and (C) All events obtained from time-lapse image sequence acquired in examining microtubule interaction of Kif4A-GFP (20 pM) in presence of 0, 30, 60, 100, 200 and 400 pM K401-unlabeled molecules by single particle tracking. The instantaneous velocity histograms were fit to Gaussian distributions. (D) Instantaneous velocity versus K401 concentration, obtained from Gaussian fits in (A): 0 pM (0.34 ± 0.03 μm/s, N=1628), 30 pM (0.25 ± 0.02 μm/s, N=2108), 60 pM (0.25 ± 0.01 μm/s, N=4725), 100 pM (0.24 ± 0.01 μm/s, N=1912), 200 pM (0.22 ± 0.01 μm/s, N=6114) and 400 pM (0.20 ± 0.01 μm/s, N=3521). (E) Instantaneous velocity versus K401 concentration, obtained from Gaussian fits in (C): 0 pM (0.33 ± 0.02 μm/s, N=1833), 30 pM (0.22 ± 0.02 μm/s, N=2471), 60 pM (0.23 ± 0.01 μm/s, N=5667), 100 pM (0.23 ± 0.01 μm/s, N=2000), 200 pM (0.21 ± 0.01 μm/s, N=8176) and 400 pM (0.18 ± 0.01 μm/s, N=5113). The error bars represent the standard error of the mean.

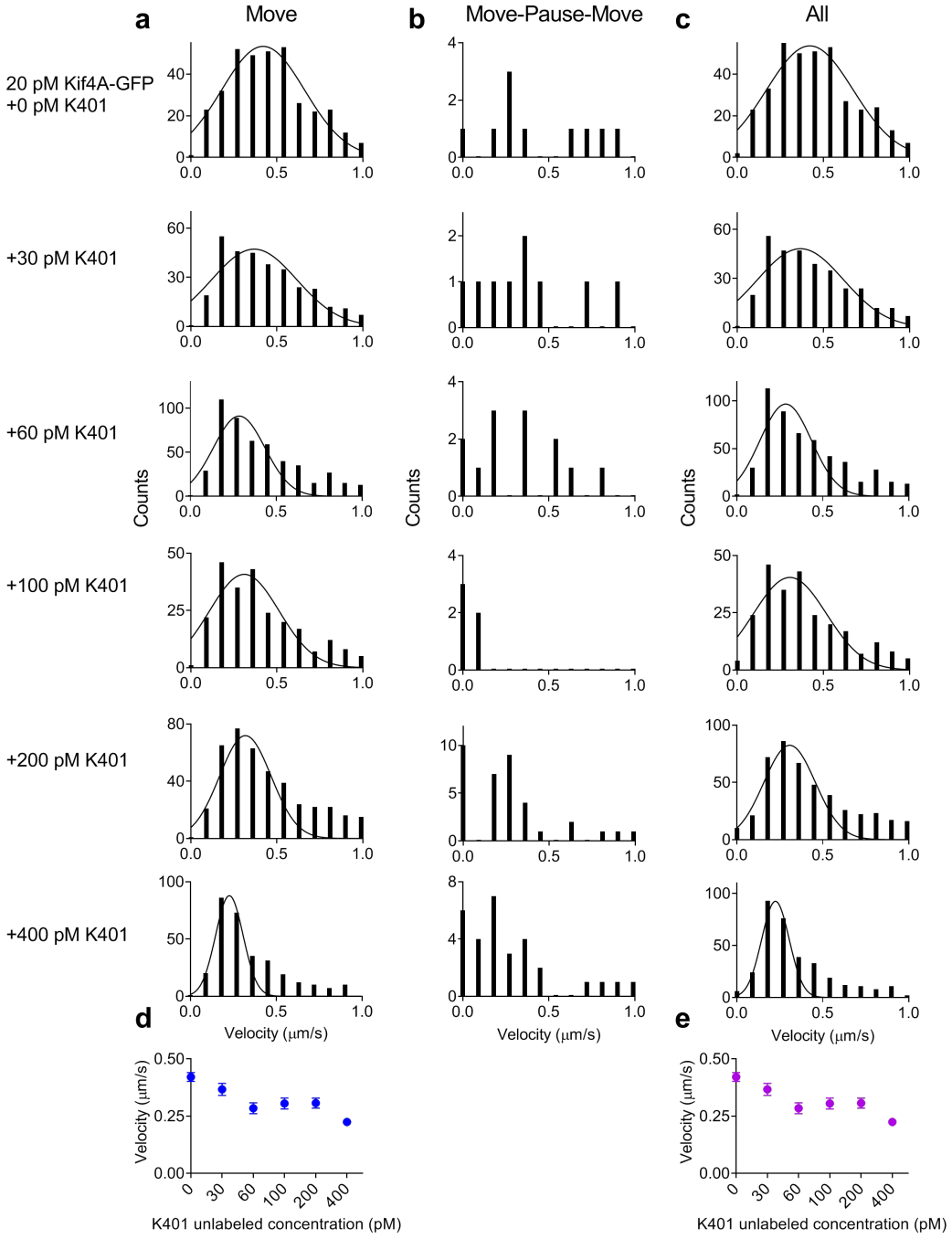

Fig. S13. Histograms of the velocity for (A) Move, (B) Move-Pause-Move and (C) All events obtained from time-lapse image sequence acquired in examining microtubule interaction of Kif4A-GFP (20 pM) in presence of 0, 30, 60, 100, 200 and 400 pM K401-unlabeled molecules by single particle tracking. The velocity histograms were fit to Gaussian distributions. (D) Velocity versus K401 concentration, obtained from Gaussian fits in (A): 0 pM (0.42 ± 0.02 μm/s, N=351), 30 pM (0.37 ± 0.03 μm/s, N=315), 60 pM (0.28 ± 0.03 μm/s, N=495), 100 pM (0.31 ± 0.03 μm/s, N=240), 200 pM (0.32 ± 0.03 μm/s, N=411) and 400 pM (0.23 ± 0.08 μm/s, N=304). (E) Velocity versus K401 concentration, obtained from Gaussian fits in (C): 0 pM (0.42 ± 0.02 μm/s, N=381), 30 pM (0.37 ± 0.03 μm/s, N=333), 60 pM (0.28 ± 0.02 μm/s, N=545), 100 pM (0.31 ± 0.02 μm/s, N=257), 200 pM (0.31 ± 0.02 μm/s, N=491) and 400 pM (0.22 ± 0.02 μm/s, N=354). The error bars represent the standard error of the mean.

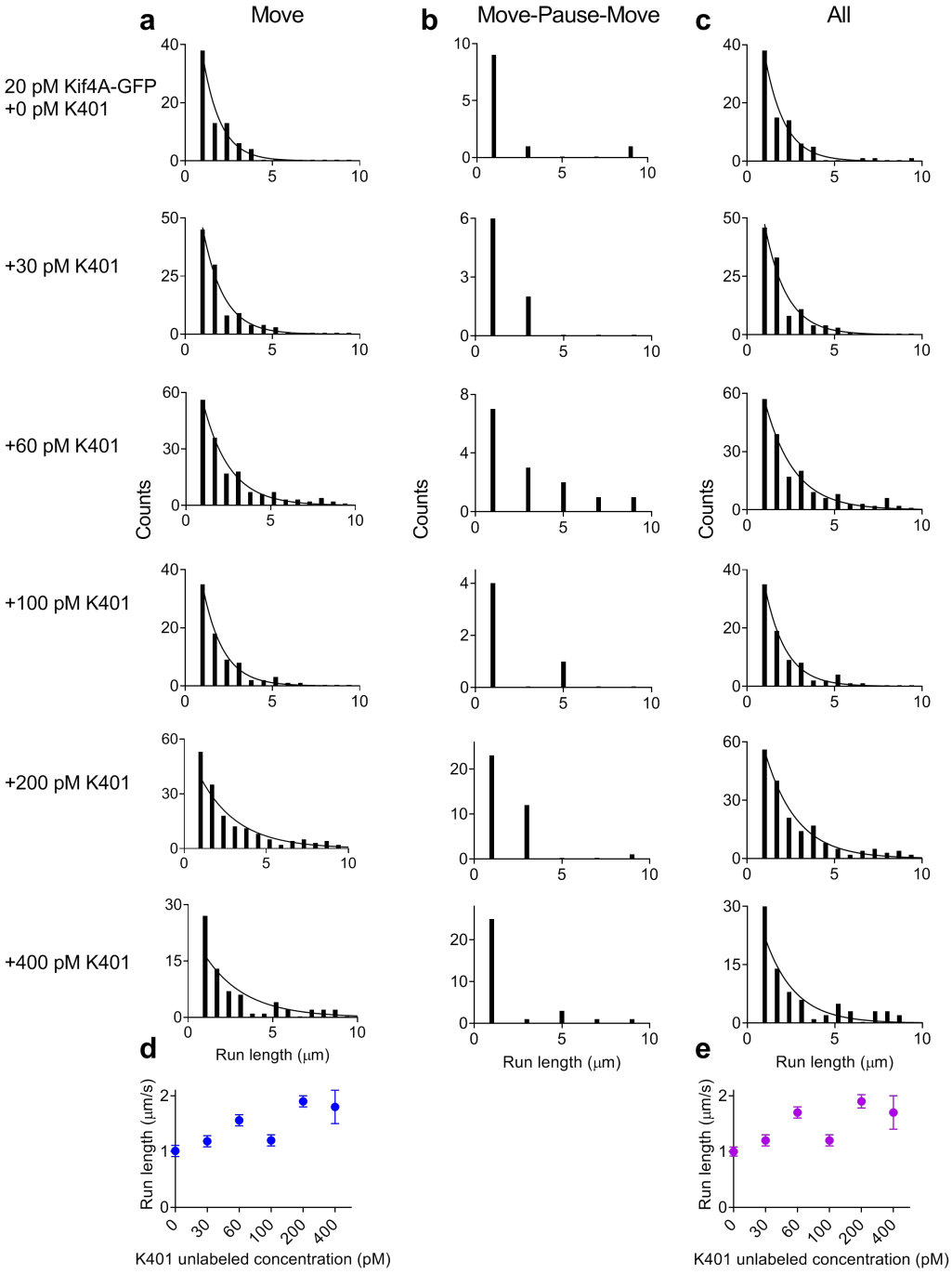

Fig. S14. Histograms of the run length for (A) Move, (B) Move-Pause-Move and (C) All events obtained from time-lapse image sequence acquired in examining microtubule interaction of Kif4A-GFP (20 pM) in presence of 0, 30, 60, 100, 200 and 400 pM K401-unlabeled molecules by single particle tracking. The run length histograms were fit to exponential fits. (D) Run length versus K401 concentration, obtained from exponentials fit in (A): 0 pM (1.0 ± 0.1 nm, N=75), 30 pM (1.2 ± 0.1 nm, N=105), 60 pM (1.6 ± 0.1 nm, N=168), 100 pM (1.2 ± 0.1 nm, N=80), 200 pM (2.3 ± 0.1 nm, N=165) and 400 pM (2.4 ± 0.5 nm, N=69). (E) Run length versus K401 concentration, obtained from exponentials fits in (C): 0 pM (1.1 ± 0.1 nm, N=82), 30 pM (1.2 ± 0.1 nm, N=111), 60 pM (1.7 ± 0.1 nm, N=179), 100 pM (1.2 ± 0.1 nm, N=82), 200 pM (1.9 ± 0.1 nm, N=186) and 400 pM (1.7 ± 0.3 nm, N=79). The error bars represent the standard error of the mean.

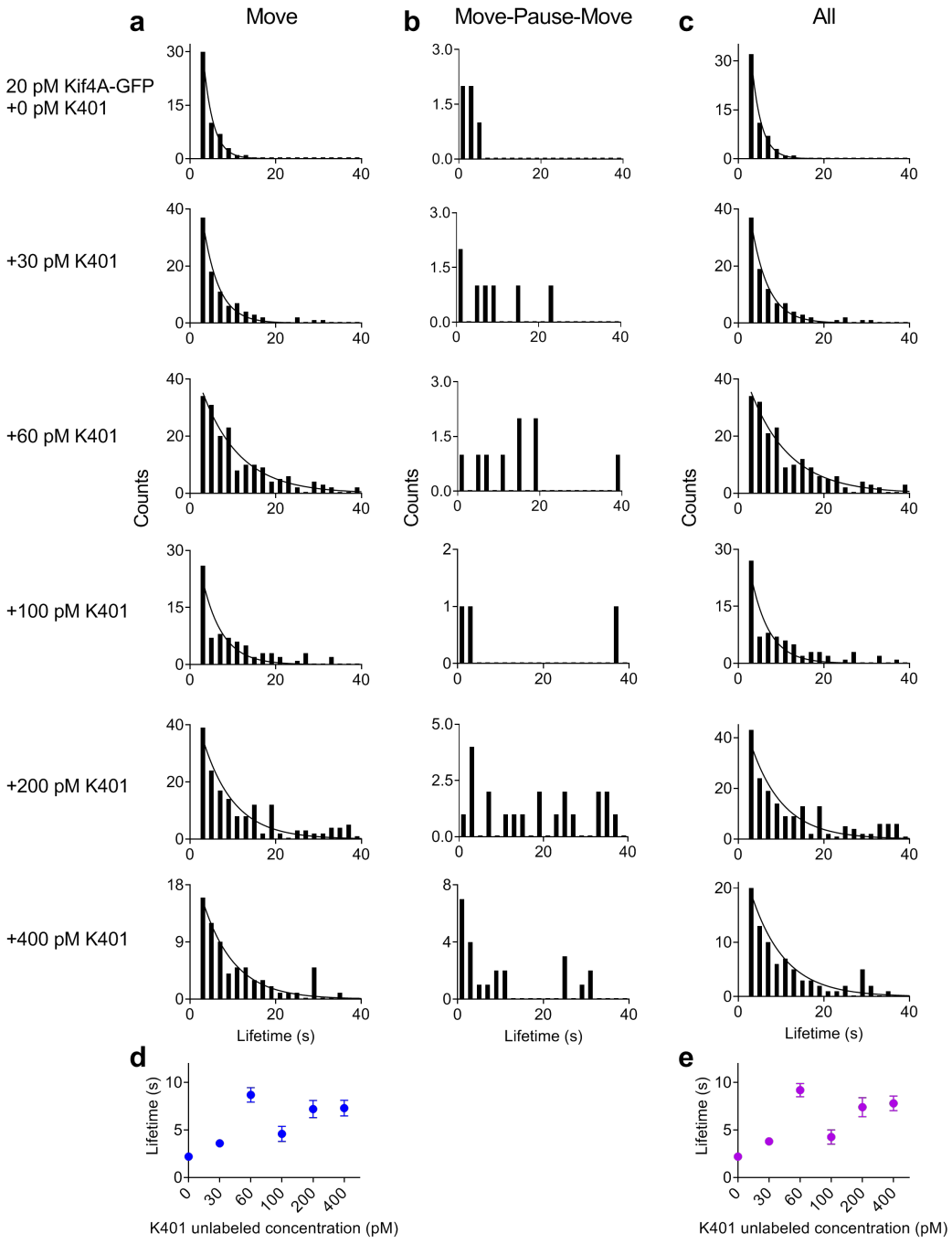

Fig. S15. Histograms of the lifetime for (A) Move, (B) Move-Pause-Move and (C) All events obtained from time-lapse image sequence acquired in examining microtubule interaction of Kif4A-GFP (20 pM) in presence of 0, 30, 60, 100, 200 and 400 pM K401-unlabeled molecules by single particle tracking. The lifetime histograms were fit to exponential fits. (D) Lifetime versus K401 concentration, obtained from exponential fits in (A): 0 pM (2.2 ± 0.1 s, N=52), 30 pM (3.6 ± 0.2 s, N=92), 60 pM (8.8 ± 0.7 s, N=173), 100 pM (4.6 ± 0.8 s, N=75), 200 pM (7.2 ± 0.9 s, N=162) and 400 pM (7.3 ± 0.8 s, N=68). (E) Lifetime versus K401 concentration, obtained from exponential fits in (C): 0 pM (2.2 ± 0.1 s, N=55), 30 pM (3.8 ± 0.2 s, N=97), 60 pM (9.2 ± 0.7 s, N=181), 100 pM (4.3 ± 0.8 s, N=77), 200 pM (7.4 ± 1.0 s, N=181) and 400 pM (7.8 ± 0.8 s, N=81). The error bars represent the standard error of the mean.

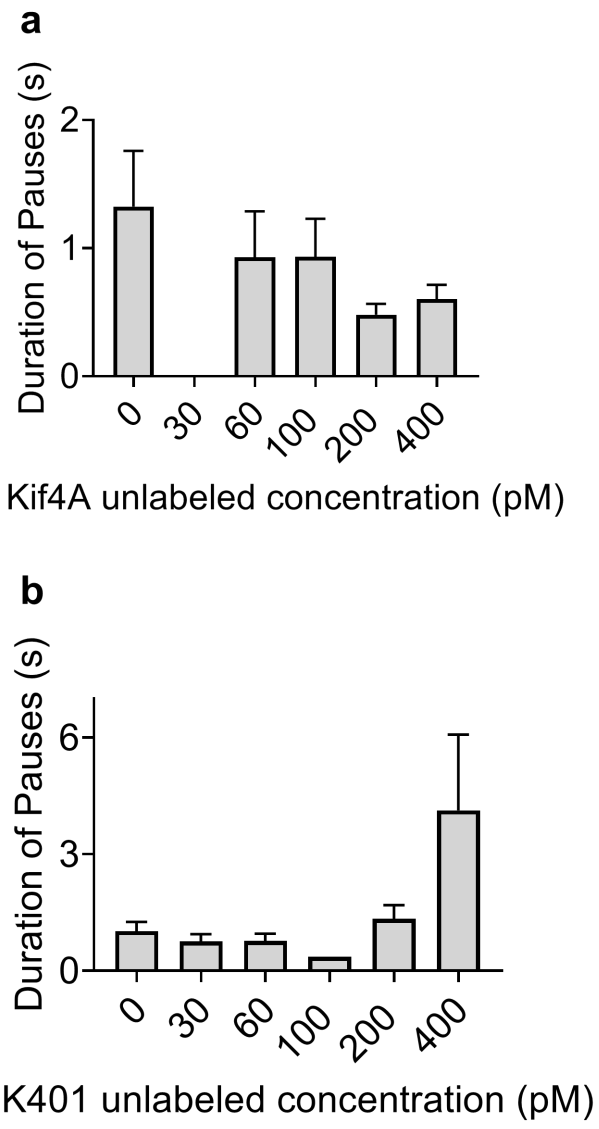

Fig. S16. Duration of pauses in Move-Pause-Move events as a function of (A) Kif4A or (B) K401 unlabeled concentration. Move-Pause-Move events were determined by single particle tracking analysis (see supplementary methods). In each Move-Pause-Move event, the time spent in the 'Pause' is determined.

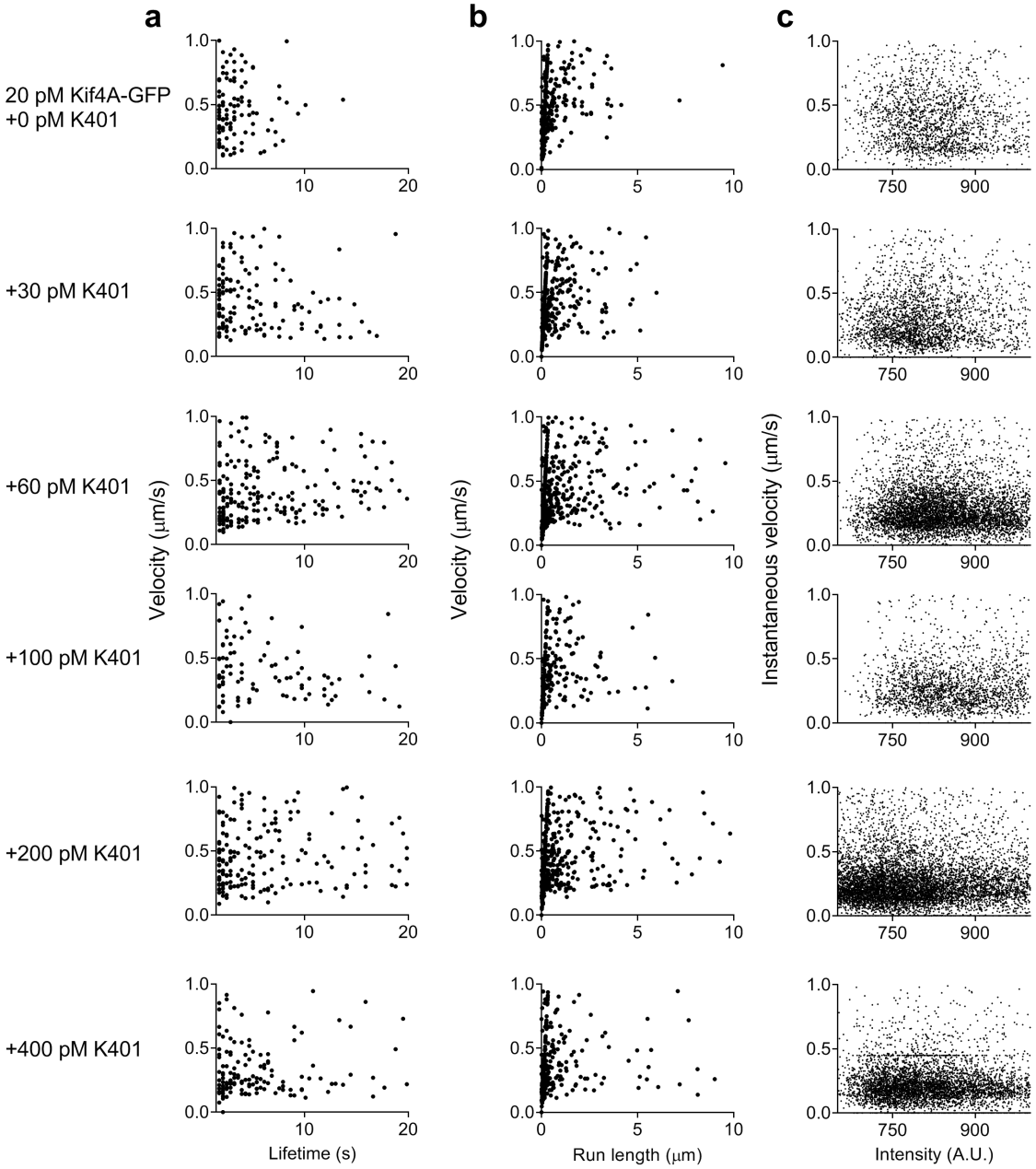

Fig. S17. (A) Velocity versus lifetime, (B) velocity versus run length, and (C) Instantaneous velocity versus intensity of 20 pM Kif4A-GFP in the presence of an increasing amount of unlabeled K401 (0-400 pM) obtained from analyzing experimental data using single particle tracking (see supplementary methods).

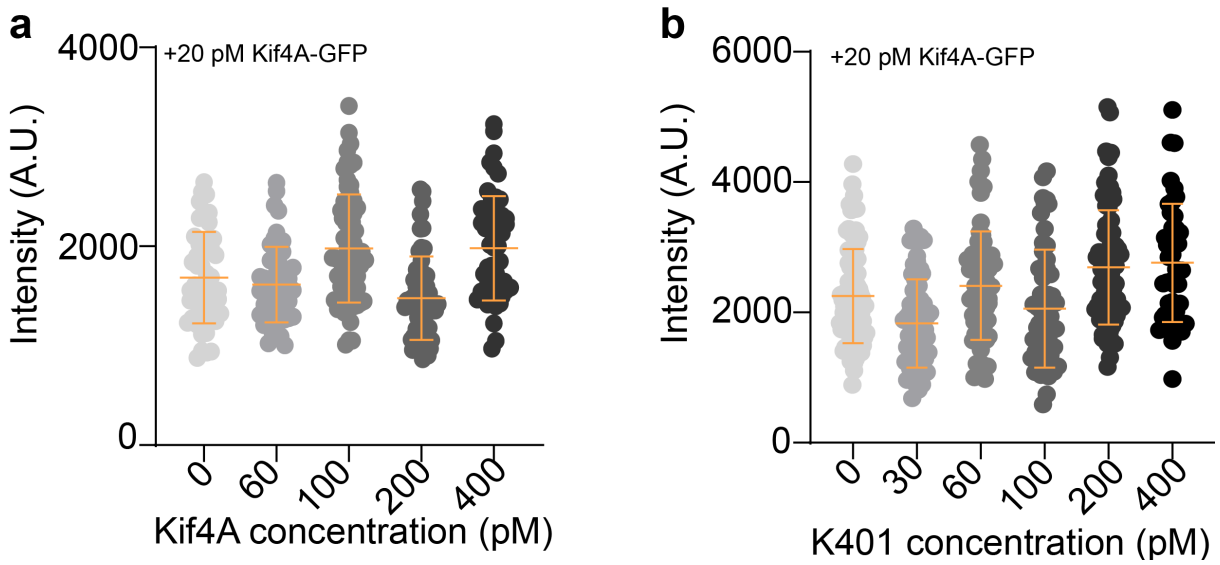

Fig. S18. Single molecule GFP intensity distributions with (A) unlabeled Kif4A concentrations 0-400 pM (from experiments in Fig. 2A) and (B) unlabeled K401 concentrations 0-400 pM (from experiments in Fig. 3A) in the presence of 20 pM Kif4A-GFP obtained by kymograph analysis (see kymograph image analysis in supplementary methods). The error bars represent the standard error.

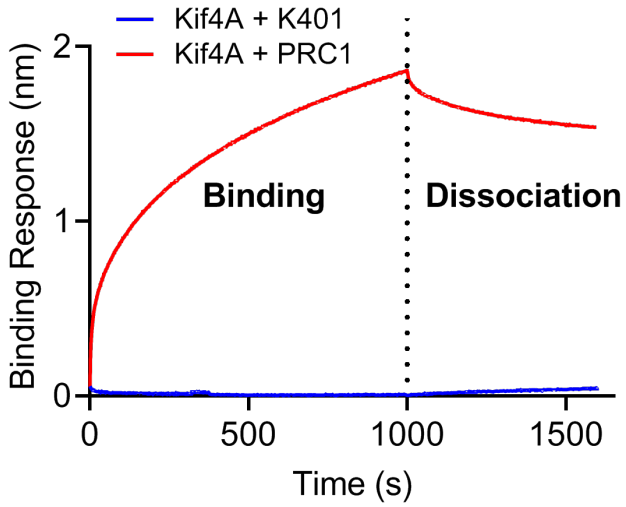

Fig. S19. Representative BLI sensorgram of the binding response of 500 nM Kif4A-GFP in solution to immobilized K401 (blue) or PRC1 (red) (see supplementary methods). Vertical dotted line indicates the binding and dissociation phases. The sensorgrams have been corrected for drift from the sensor and non-specific binding of Kif4A to the sensor.

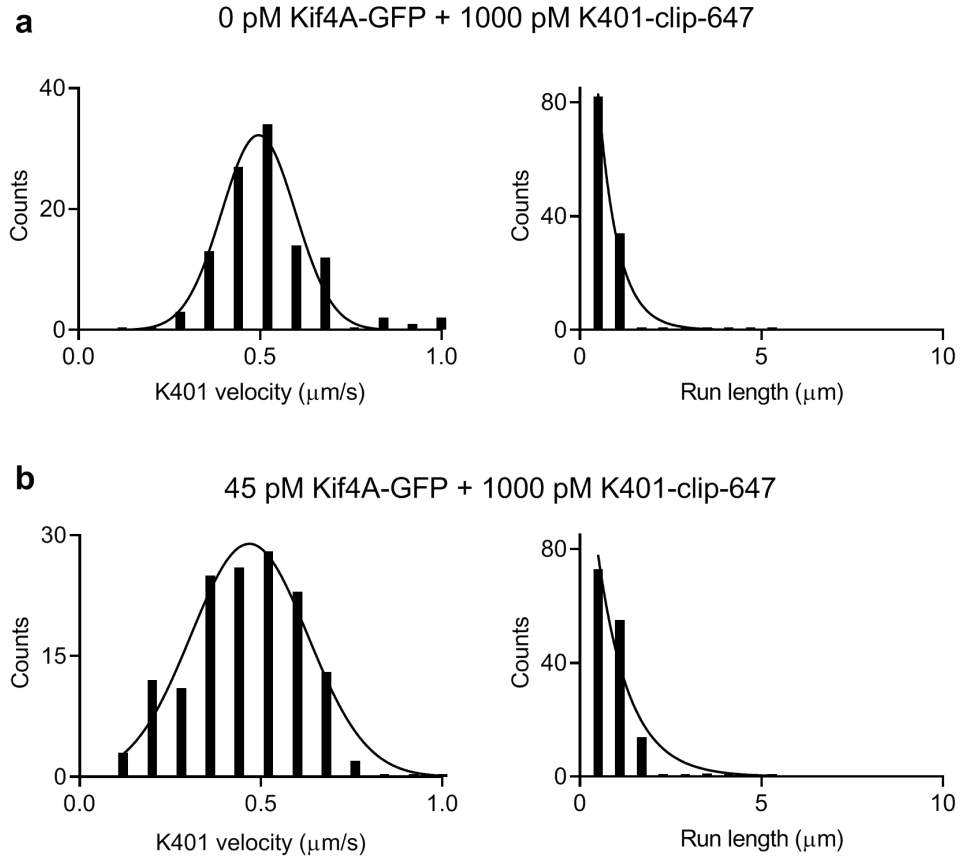

Fig. S20. Quantification of K401 velocity and run length in the (A) absence and (B) presence of Kif4A. Histograms for (A) 0 pM Kif4A-GFP + 1000 pM K401-clip-647 (Average velocity: 0.50 ± 0.01 μm/s, N=143; Run length: 0.85 ± 0.2 um, N=143) and (B) 45 pM Kif4A-GFP + 1000 pM K401-clip-647 (Average velocity: 0.46 ± 0.01 μm/s, N=108; Run length: 0.55 ± 0.1 μm, N=116). The mean and SEM are determined by the Gaussian fit for the velocity histogram and exponential fit for the run length distribution.

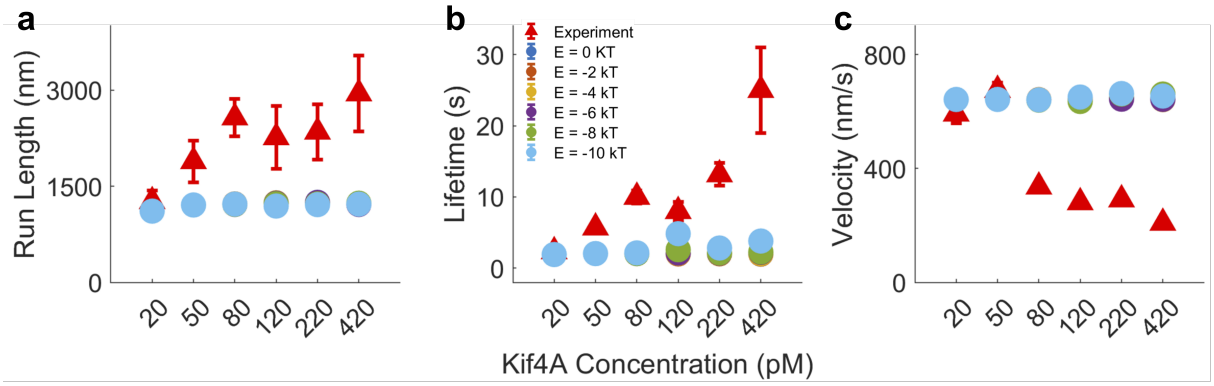

Fig. S21. (A) Run length, (B) lifetime and (C) velocity versus Kif4A concentration from simulations with varying energy of short-range interaction (circles) and experiment (triangles). Simulation data points represent the average of four independent runs. Error bars represent the error of the mean.

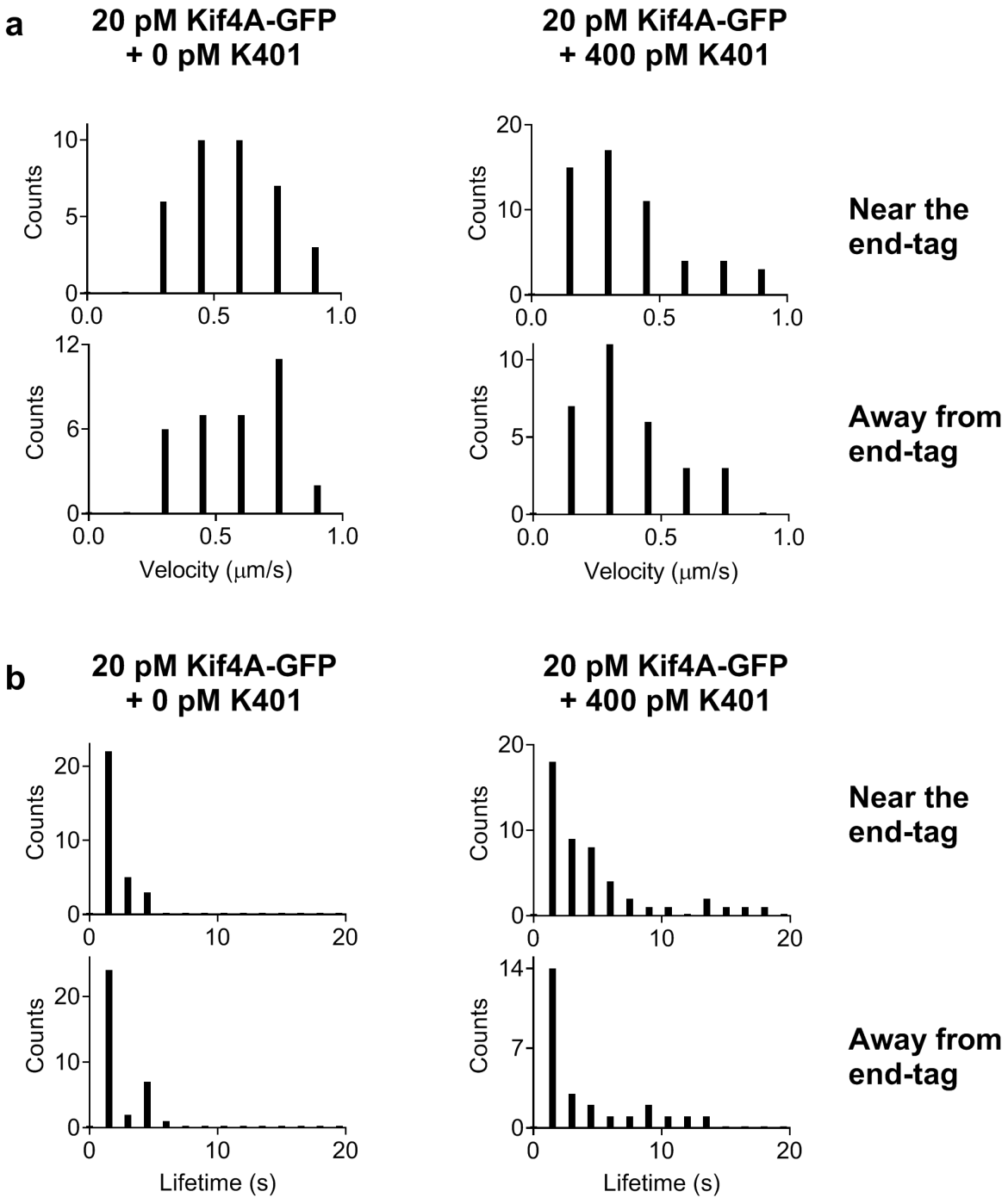

Fig. S22. Histograms of the (A) velocity and (B) lifetimes near or away from the end-tag on microtubules. 'Near the end-tag' refers to events in the half of the microtubule that includes the end-tag, and 'Away from the end-tag' refers to events in the half of the microtubule that does not include the end-tag. (A) Near the end-tag; 20 pM Kif4A-GFP + 0 pM K401, N=36; 20 pM Kif4A-GFP + 400 pM K401, N=56; Away from the end-tag; 20 pM Kif4A-GFP + 0 pM K401, N=36; 20 pM Kif4A-GFP + 400 pM K401, N=32. (B) Near the end-tag; 20 pM Kif4A-GFP + 0 pM K401, N=30; 20 pM Kif4A-GFP + 400 pM K401, N=48; Away from the end-tag; 20 pM Kif4A-GFP + 0 pM K401, N=34; 20 pM Kif4A-GFP + 400 pM K401, N=26).

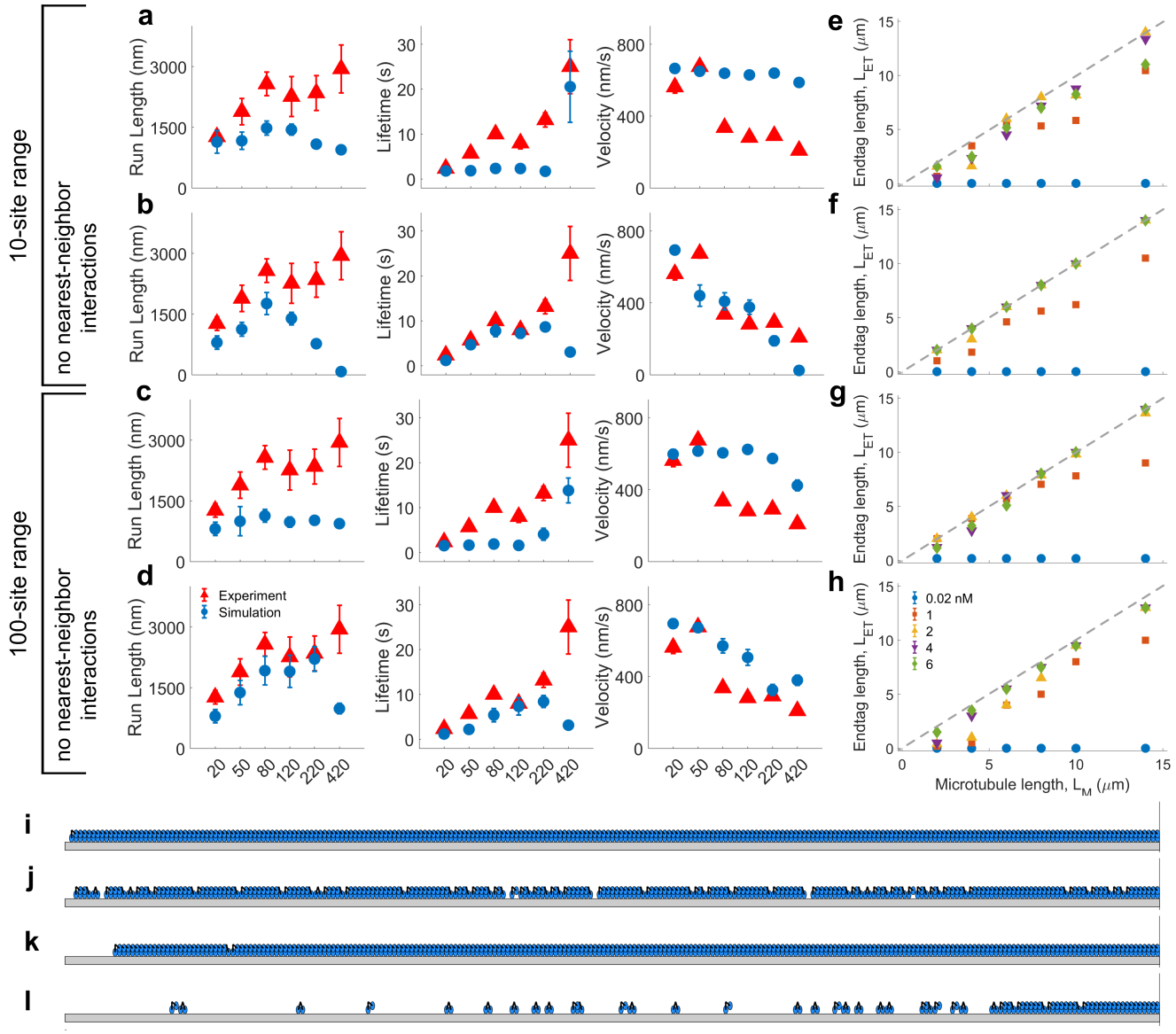

Fig. S23. (A-D) Best-fit motility data for simulations optimized with the range of "long-range" interactions fixed to 10 sites (A-B) and 100 sites (C-D). In both cases, data are shown with nearest-neighbor interactions (A, C) and without nearest-neighbor interactions (B, D). The best-fit parameters for a fixed range of 10 sites and nearest-neighbor interactions active (A) are an interaction strength of 8.5 kT and a saturation energy of 8.5 kT. When nearest-neighbor interactions are turned off (B), the best-fit parameters remain the same. The best-fit parameters for a fixed range of 100 sites and nearest-neighbor interactions active (C) are an interaction strength of 4.5 kT and a saturation energy of 7.5 kT. When nearest-neighbor interactions are turned off (D), the best-fit parameters are an interaction energy of 5.5 kT and a saturation energy of 5.5 kT. (E-H) Corresponding end-tag versus microtubule length plots using the same parameters as the motility plots they appear next to. The dashed gray lines have a slope of 1 and represent full saturation of the microtubule lattice with bound motors. (I-L) Snapshots of simulation movies for a 2-μm-long microtubule at 1 nM bulk concentration corresponding to end-tag plots E-H, respectively.

Table S1. Parameters used in our simulation. Values shown correspond to the best-fit model that includes nearest-neighbor interactions, long-range binding interactions, and long-range stepping interactions (Fig. 5J-L). The version of the model without the long-range stepping interaction (Fig. 5F-H) uses values of 9.6 μm, 1.3 $k_{\mathrm{B}}T$, and 4.0 $k_{\mathrm{B}}T$ for the quadratic potential cutoff, strength, and ceiling, respectively. The nearest-neighbor energy is 1.75 $k_{\mathrm{B}}T$ in this model version. For a more detailed discussion, see Ref. 1.

	Description	Value	Notes
General			
$k_{\mathrm{B}}T$	Thermal energy	4.1 pN·nm	Room temperature
t	Total simulation time	$5 - 180$ min	Longer time for lower motor density
t_{e}	Pre-equilibration time	100 s	Time before equilibration status is checked
t_{c}	Equilibration check interval	10 s	Data window for equilibration statistics
t_{s}	Data snapshot interval	$0.01 - 0.1$ s	Time between data output
dt	Timestep	2×10^{-5} s	Time that passes each kMC step
Microtubules			
L	Length	$0.1 - 20$ μm	Experimental values
Δ	Site size	8.2 nm	Tubulin dimer length
Motors			
k_{on}	Per-site binding rate	3.6×10^{-4} (nM·s)$^{-1}$	Estimated from 20 pM kymographs
c	Bulk concentration	$0.02 - 6.0$ nM	Experimental values
c_{eff}	Effective concentration of unbound head while motor is singly bound	4×10^{6} nM	Assumes that the unbound head can explore a quarter-sphere of radius 7.5 nm
k_{ATP}	ATP binding rate	5000 s^{-1}	Taken from Ref. 3
k_{hydro}	ATP hydrolysis rate	95 s^{-1}	Sets baseline velocity to ∼600 nm/s
$k_{\mathrm{off},1}$	Singly bound off rate	8 s^{-1}	Sets baseline processivity to ∼1.2 μm
$k_{\mathrm{off},2}$	Doubly bound off rate	260 s^{-1}	Taken from Ref. 3
Motors - binding cooperativity			
ϵ	Nearest-neighbor energy	1.6 $k_{\mathrm{B}}T$	Best-fit value; see Ref. 1
D	Quadratic potential cutoff	8 μm	Best-fit value; see Ref. 1
E_0	Quadratic potential strength	0.95 $k_{\mathrm{B}}T$	Best-fit value; see Ref. 1
E^*	Quadratic potential ceiling	4.75 $k_{\mathrm{B}}T$	Best-fit value; see Ref. 1
Motors - stepping cooperativity			
F_{int}	Internal necklinker tension	26 pN	Taken from Ref. 3
δ_{off}	Unbinding distance parameter	0.13 nm	Best-fit value; compare to 0.35 nm for kinesin-1 from Ref. 3
δ_{ATP}	ATP binding distance parameter	1.2 nm	Best-fit value; compare to 4.6 nm for kinesin-1 from Ref. 3

Movie S1. Simulated fluorescence microscopy movie of a 10-μm-long microtubule with 80 pM Kif4A. The brightness of motors is chosen to make individual motors clearly visible.

Movie S2. Simulated fluorescence microscopy movie of a 10-μm-long microtubule with 120 pM Kif4A. The brightness of motors is chosen to make individual motors clearly visible. A cascade of binding events can be observed around t = 375 s. This type of cascade is not seen anywhere in the ∼10,000 second run time of the 80 pM simulation in Movie S1.

Movie S3. Occupancy profile of an 8-μm-long microtubule evolving over time. The red horizontal line indicates the end-tag boundary as defined by our automated algorithm.

References

1. SA Fiorenza, DG Steckhahn, MD Betterton, Modeling spatiotemporally varying protein–protein interactions in CyLaKS, the Cytoskeleton Lattice-based Kinetic Simulator. *The Eur. Phys. J. E* **44** (2021).
2. SA Fiorenza, CyLaKS v1.0 (https://github.com/Betterton-Lab/CyLaKS) (2021).
3. JO Andreasson, et al., Examining kinesin processivity within a general gating framework. *eLife* **4**, e07403 (2015).
4. R Subramanian, J Gelles, Two Distinct Modes of Processive Kinesin Movement in Mixtures of ATP and AMP-PNP. *J. Gen. Physiol.* **130**, 445–455 (2007).
5. R Subramanian, SC Ti, L Tan, SA Darst, TM Kapoor, Marking and Measuring Single Microtubules by PRC1 and Kinesin-4. *Cell* **154**, 377–390 (2013).